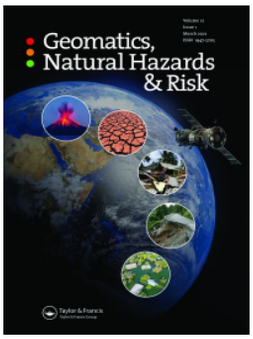

Geomatics, Natural Hazards and Risk

ISSN: 1947-5705 (Print) 1947-5713 (Online) Journal homepage: www.tandfonline.com/journals/tgnh20

Landslide susceptibility mapping based on data mining models in Lesser Caucasus and Kura foreland basin (Armenia and Azerbaijan)

Israr Ullah , Klaus Reicherter , Tomáš Pánek , Alessandro Tibaldi , Husam Al-Najjar , Bahareh Kalantar, Naonori Ueda & Hans-Balder Havenith

To cite this article: Israr Ullah , Klaus Reicherter , Tomáš Pánek , Alessandro Tibaldi , Husam Al-Najjar , Bahareh Kalantar, Naonori Ueda & Hans-Balder Havenith (2025) Landslide susceptibility mapping based on data mining models in Lesser Caucasus and Kura foreland basin (Armenia and Azerbaijan), Geomatics, Natural Hazards and Risk, 16:1, 2537221, DOI: 10.1080/19475705.2025.2537221

To link to this article: https://doi.org/10.1080/19475705.2025.2537221

Published online: 17 Aug 2025.

GEOMATICS, NATURAL HAZARDS AND RISK
2025, VOL. 16, NO. 1, 2537221
https://doi.org/10.1080/19475705.2025.2537221

Landslide susceptibility mapping based on data mining models in Lesser Caucasus and Kura foreland basin (Armenia and Azerbaijan)

Israr Ullah[a], Klaus Reicherter[a], Tomáš Pánek[b], Alessandro Tibaldi[c], Husam Al-Najjar[d], Bahareh Kalantar[e], Naonori Ueda[e] and Hans-Balder Havenith[f]

[a]Institute of Neotectonics and Natural Hazards, RWTH Aachen University, Aachen, Germany; [b]Department of Physical Geography and Geoecology, Faculty of Science, University of Ostrava, Ostrava, Czech Republic; [c]Department of Earth and Environmental Sciences, University of Milan-Bicocca, Milan, Italy; [d]School of Computer Science, Faculty of Engineering and IT, University of Technology Sydney, Sydney, NSW, Australia; [e]RIKEN Center for Advanced Intelligence Project, Disaster Resilience Science Team, Tokyo, Japan; [f]Georisk & Environment, Department of Geology, University of Liege, Liege, Belgium

ABSTRACT

Landslides are a major geological hazard causing significant loss of life and infrastructure damage worldwide. Landslide susceptibility mapping is a crucial, though developing, tool for understanding the spatial distribution of landslide hazard. This study addresses the absence of a comprehensive landslide inventory, limited understanding of causative factors and the lack of regional-scale susceptibility maps for the Lesser Caucasus and Kura Basin (LC-KB). A landslide inventory was created for the Lesser Caucasus of Azerbaijan and compiled with other inventories, documenting 3,659 landslide polygons. Sixteen causative factors were analysed, and multicollinearity tests confirmed no significant correlations. Three Machine Learning (ML) models—Logistic Regression (LGR), Support Vector Machine (SVM) and Extreme Gradient Boosting (XGBoost)—were fine-tuned to create landslide susceptibility maps. Slope is consistently the most influential factor across all models. Results suggest stronger influence of seismic factors than climatic ones. XGBoost achieves the highest accuracy (0.81) on the testing data set, followed by SVM (0.80) and LGR (0.73). The first two models show strong validation performance, with AUC values of 0.89 and 0.87, respectively, while LGR shows a lower AUC of 0.78. The results are vital for planning and disaster management, highlighting areas needing urgent mitigation.

ARTICLE HISTORY
Received 24 March 2025
Accepted 12 July 2025

KEYWORDS
Landslide susceptibility; GIS; remote sensing; machine learning; data mining; logistic regression; support vector machine; extreme gradient boosting

1. Introduction

Landslides are among the most common geophysical hazards, with approximately 66 million people living in areas prone to landslide risk (Sim et al. 2022). Additionally, landslides incur substantial economic losses, estimated at $8 billion globally (Wallemacq et al. 2018). Landslides manifest in various forms, including those induced by seismic and volcanic activity, precipitation or human activities (Samia et al. 2017). Landslides susceptibility (LS) refers to the probability of a landslide occurring in an area due to various geological and environmental factors (Guzzetti et al. 2006). LS assessment, which involves landslide identification, prediction of occurrence and modelling, is the fundamental part of a comprehensive landslide study. The occurrence of landslides presents a multifaceted investigation challenge involving the gravitational mass movement influenced by a multitude of local and regional factors such as geomorphology, hydrology, anthropogenic, climatic conditions and tectonics (Hassangavyar et al. 2020). Therefore, combining geoscientific data with data mining techniques for studying and delineating landslide-susceptible zones enhances scientific knowledge and supports practical applications for mitigating landslide impacts.

CONTACT Bahareh Kalantar bahareh.kalantar@riken.jp

A well-compiled landslide inventory is crucial for understanding spatial patterns alongside different Causative Factors (CFs) needed for LS mapping. Landslide identification for inventory mapping techniques can be broadly classified into conventional and recently developed advanced techniques (Mohan et al. 2022). The traditional methods include geomorphological field mapping and visual interpretation of aerial photographs or other remote sensing (RS) imageries to identify landslides and monitor landslide activity by installing field equipment or taking periodical field measurements (Santangelo et al. 2015). Visual and semiautomated interpretation of earth observation (EO) images supported by adequate field validation is currently the most widely used method for making landslide inventories (Kothyari et al. 2022). However, despite recent technological advancements, visual interpretation of satellite imagery remains the most common method to prepare landslide inventory (Santangelo et al. 2015). Although this method is time consuming, the accuracy of delineating landslides is higher than the semiautomated methods (Justice 2021).

LS analysis is attempted through quantitative, semi-quantitative and qualitative methods (Huang et al. 2024). Quantitative multivariate statistical models, such as machine learning (ML) techniques, offer a promising solution for nonlinear geographical modelling (Conforti et al. 2012). ML techniques are broadly categorised into supervised and unsupervised algorithms. Supervised ML techniques, including Extreme Gradient Boosting (XGBoost) (Zhang et al. 2023), Linear Regression (LR) (Pourghasemi et al. 2013), Logistic Regression (LGR) (Akgun 2012), Support Vector Machines (SVM) (Huang and Zhao 2018) and Convolution Neural Network (CNN) (Aslam et al. 2021), rely on labelled data to infer patterns.

Conversely, unsupervised ML techniques can uncover inherent data structures without labels. Commonly used unsupervised ML algorithms in LS analysis include k-means clustering, principal component analysis (PCA) analysis (Xu et al. 2024), clustering (Wang et al. 2017) and Gaussian Mixture Models (GMM) (Zhou et al. 2020). The plethora of ML-based LS analyses may overwhelm researchers when selecting the appropriate algorithm. Therefore, numerous researchers (Pourghasemi et al. 2013; Micheletti et al. 2014) have highlighted the superiority of supervised ML algorithms. This study focuses on quantitative methods that utilise statistic-probabilistic-based data mining models to assess the role of landslide CFs. For many countries, the available landslide inventories are not detailed enough to support statistical analyses at a broader scale. Consequently, researchers commonly use heuristic methods to generate qualitative LS maps for large regions with the limited inventory data (Gaprindashvili and Van Westen 2016).

The Lesser Caucasus and Kura Basin (LC-KB) is the perfect region for using data mining models to assess the LS, as it hosts hundreds of shallow and deep-seated landslides of possible seismic origin and climatic influence (Fomenko et al. 2021; Kumar et al. 2021; Havenith et al. 2022). Different studies in this area have recently highlighted the combined seismic and climatic influence on landslide occurrences (Matossian et al. 2020; Pánek et al. 2024). Both the seismic and climatic factors dominate and contribute more to landslide initiation in the Greater Caucasus (Gaprindashvili and Van Westen 2016; Fomenko et al. 2021), which matches with the seismic and climatic conditions of many mountains in the Alpine-Himalayan belt (Velayudham et al. 2021). On the other hand, in the Lesser Caucasus, the seismotectonic and also volcanic conditions have a more substantial influence on landslide activity due to the prevalent semiarid climate (Matossian et al. 2020). Several researchers have conducted studies on LS in the Caucasus region, but most have focused on specific areas on a smaller scale and have relied solely on statistical models considering a limited number of CFs. Recent research by Ledworowska et al. (2020) compared the effectiveness of artificial neural networks (ANN) and C5.0 decision tree models in analysing LS in Armenia. The results indicated that the ANN models outperformed the C5.0 models, providing more accurate and reliable results. The C5.0 models were deemed unsuitable for susceptibility analysis due to overfitting and pruning artefacts. Another study by Tsereteli et al. (2019) focused on the hazard risk of debris/mudflow events in Georgia. Meanwhile, Alcaraz Tarragüel et al. (2012) analysed the impact of avalanches and landslides on cultural heritage in Georgia using Spatial Multicriteria Evaluation (SMCE). As it is evident from existing research on LS in LC-KB that most of research is mostly focused on small areas with the limited inventories, using traditional methods. This study addresses these gaps by producing one of the first regional-scale susceptibility maps for the LC-KB.

Furthermore, Gaprindashvili and Van Westen (2016) presented a methodology for creating a national landslide hazard and risk map for Georgia utilising SMCE to generate a qualitative landslide risk index. Another study by Matossian et al. (2020) analysed the distribution of landslides over the Armenian Lesser Caucasus with a total of 1,036 landslides mapped through manual digitisation using Google Earth imagery.

Previous studies in the focused research area have mainly used statistical methods for LS, leaving a gap in exploring the potential of data mining models. This creates an opportunity to investigate how employing these advanced models affects prediction accuracy in LS. Thus, this research endeavours to fill in the research gap by creating and compiling a comprehensive landslide inventory for the LC-KB. This study aims to map the distribution of landslides across the region and establish a statistical database of these occurrences. Additionally, the primary aim of this study is to develop one of the first robust regional-level LS maps using grid search-based fine-tuned data mining models. In particular, the study implements classification and regression approaches with LGR, SVM and XGBoost models to develop appropriate LS maps for the LC-KB.

2. Study area

The LC-KB (Armenia, Azerbaijan and Georgia) are bounded in the west by the Black Sea and Eastern Anatolia (Turkey), in the north by the Greater Caucasus (Georgia and Russia), and in the east by the Caspian Sea. The LC-KB lies within a geologically complex zone shaped by ongoing continental collision. The Lesser Caucasus explicitly displays a strong influence of lithospheric anisotropies like ophiolitic sutures and faults demarcating continental blocks formed through terrane accretion due to Arabian and Eurasian plate collision (Avagyan et al. 2005). The two fold-and-thrust belts, the Greater and Lesser Caucasus, are divided by the Caspian-Kura Intermontane Depression in the eastern section in Azerbaijan (Adamia et al. 2010), as shown in Figure 1.

The Kura Basin is filled primarily by a Neogene sedimentary sequence. Neogene and Quaternary sediments dominate the basin, thickening eastward (Nalivkin 1976; Forte et al. 2015). Additionally, it is a zone of intense shortening accommodating ~30%–40% of the total convergence between Arabia and Eurasia since ~2–3 Ma (Forte et al. 2010). On the other hand, the Lesser Caucasus region in Armenia is dominated by volcano-sedimentary sequences (KoçyİğİT et al. 2000). Consequently, Armenia faces exposure to volcanic hazards and associated secondary gravitational effects.

Along with morphostructural and lithological heterogeneities of LC-KB, the high landslide proneness is also attributed to high seismicity, particularly in the LC. The Pambak-Sevan-Sunik Fault (PSSF), Armenia's longest fault (490 km) segmented into five parts, is responsible for notable destructive earthquakes in 915, 1187, 1407, 1853 and 1931 exceeding $M \geq 6.0$ (McKenzie 1972; Karakhanian et al. 1997; Shebalin and Tatevossian 1997). The Pambak-Sevan-Sunik Fault (PSSF, 490 km long), is responsible for destructive earthquakes exceeding $M \geq 6.0$ (McKenzie 1972; Karakhanian et al. 1997). Other significant faults include the 200 km long, dextral strike-slip reverse Garni Fault (GF) and the blind Yerevan Fault (Avagyan et al. 2018).

The Kura fold and thrust belt are characterised by NW-SE striking thrust faults dipping north (Forte et al. 2010; 2013). Examples include the Mingachevir and Kura thrusts, with the latter forming the southern margin of the belt (Nalivkin 1976; Forte et al. 2010; Tibaldi et al. 2024). The instrumental seismicity lacks records of strong earthquakes ($M > 6$) within the KB (Telesca and Chelidze 2018). The largest historical earthquake ($M \sim 7.5$, 1139 CE) accumulated seismic moment tensor suggests a slower than expected deformation rate in the Caucasus, potentially indicating a significant aseismic component (Philip et al. 1989).

The Kura River meanders approximately 1,515 km through the KB between the Greater and Lesser Caucasus before converging with the tributary of the Aras River as it flows into the Caspian Sea (Hoogendoorn et al. 2005). The climate in the Caucasus is highly diverse as the Greater Caucasus (GC) acts as a climatic barrier, restricting the northward influx of colder continental air masses. In contrast, the Lesser Caucasus partially restricts the southward penetration of dry and warm air masses (Urushadze and Ghambashidze 2013). This phenomenon contributes to the aridity observed, especially within the central part of the target region.

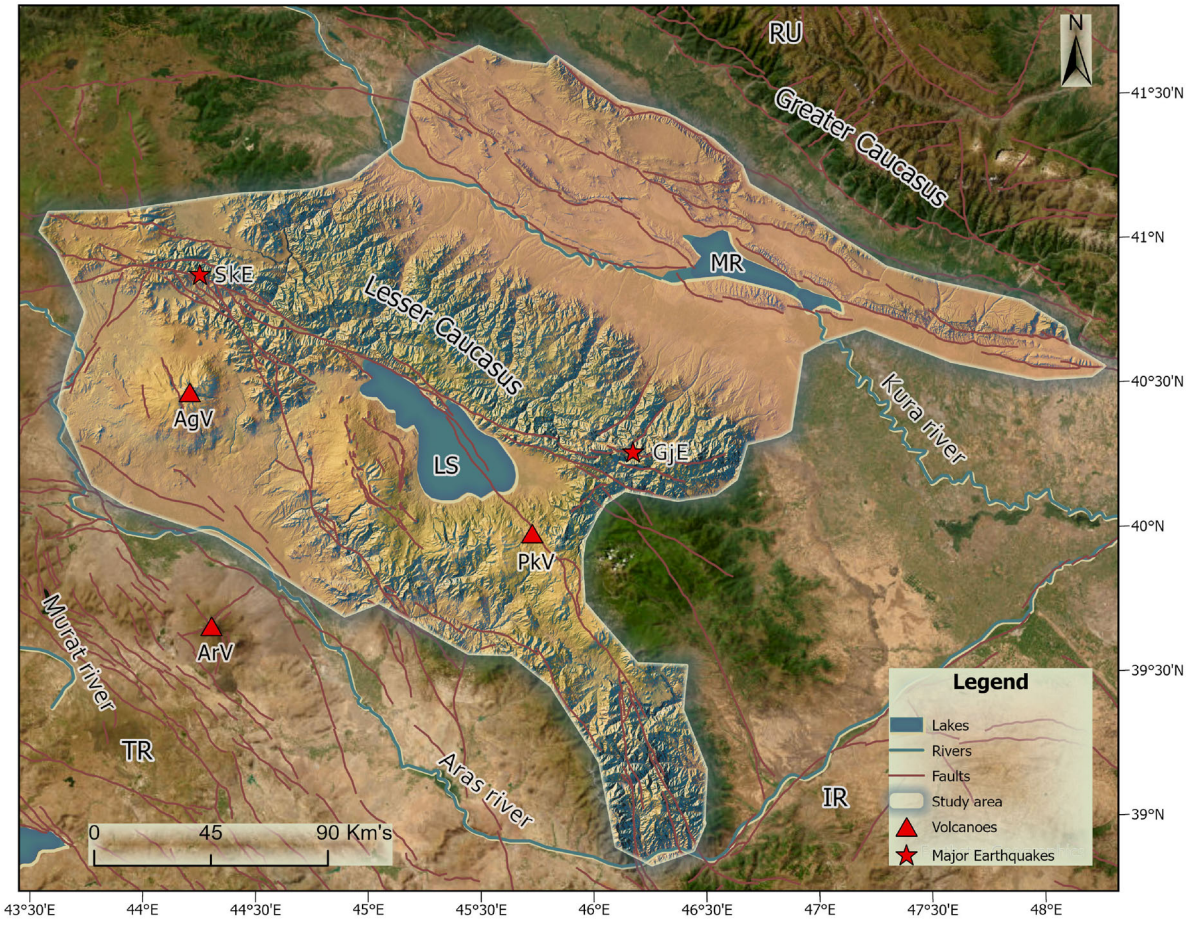

Figure 1. Location map of the study area, highlighting its diverse morphological features in Armenia and Azerbaijan. The map illustrates the bordering countries: Russia (RU), Turkey (TR) and Iran (IR). Additionally, key geographical features like the Mingachevir Reservoir (MR), and Lake Sevan (LS) are marked. Furthermore, the triangles depict the volcanoes with Aragats volcano (Agv), Ararat volcano (ArV) and Porak volcano (PkV), while the two stars represent the major earthquakes of Ganja (GjE, 1139 CE) and Spitak (SkE, 1988).

3. Methodology

3.1. Landslide inventory

A high-quality landslide inventory is crucial for modelling LS (Khalil et al. 2022). Landslide inventory depicts the spatial distribution of past landslides, providing valuable data for analysis. The existing landslide inventories for the Armenian Lesser Caucasus include the GeoRisk and the catalogues (Matossian et al. 2020). The GeoRisk inventory, compiled by the GeoRisk Scientific Research Company, encompasses over 2,000 landslides mapped over almost 30,000 km^2 Japan International Cooperation Agency (JICA), Georisk CJSC (2006). The Matossian inventory, mapped during 2017–2018, covers all of Armenia and includes data published by Matossian et al. (2020).

Both inventories contain entries for large, ancient mass movements and more recent, active/reactivated landslides. The Matossian inventory features a higher level of precision due to its use of higher-resolution imagery in Google Earth Pro compared to the GeoRisk inventory. For the Kura Basin, a detailed landslide inventory was established by Pánek et al. (2024). This inventory, compiled through satellite imagery in Google Earth Pro, includes nearly 1,600 landslides. Landslides in the Panek inventory cover less than 1% of the area but exhibit clustering in higher elevations and steeper and rougher terrains. The inventory encompasses a wide range of landslide sizes, spanning six orders of magnitude, with the small shallow slides measuring less than 100 m^2 and the largest landslide covering 24 km^2.

This study utilises 1,547 landslides from Panek and 791 landslides from Matossian inventories after excluding moraines and smaller landslides from the respective catalogues. As no prior landslide

inventory existed for the Azerbaijan side of the Lesser Caucasus, this study involves mapping landslides in that region using Google Earth Pro. The final comprehensive inventory for the whole LC-KB region compiled the mapped Azerbaijan Lesser Caucasus landslides with the existing Matossian (Armenian Lesser Caucasus) and Panek (Kura Basin) inventories. Landslide inventories are needed for both training and testing datasets for the LS models. This compiled comprehensive inventory was utilised to produce and validate the LS map for this region.

3.2. Landslide causative factors

A large spectrum of landslide CFs makes the LC-KB landslide-prone region. The LS model relies on past events and CFs. However, defining appropriate CFs poses challenges, necessitating the use of expert knowledge and existing literature to determine landslide triggers (Kavzoglu et al. 2019; Saha et al. 2022). So far, no universally accepted method to determine condition-specific CFs has been used. Boynagryan (2009) identifies several CFs to landslide occurrences in Armenia, including convex, steep, and high slopes, the presence of weathered rocks or loose volcanic deposits, groundwater levels, active faults, seismic activity, and human activities like irrigation, construction, and deforestation.

Pánek et al. (2024) suggest that while earthquakes may have triggered landslides in the Kura fold-and-thrust belt historically, recent clusters of landslides cannot be solely attributed to seismic activity. The overlapping occurrence of old and recent landslides, including post-2009 events, was not triggered by seismicity but due to factors such as heavy rainfall, river undercutting or human activities on actively incising valleys and steeply dipping slopes on anticlinal limbs (Yetirmishli et al. 2018). Although past seismic events might have caused some mapped landslides, nearly a millennium has passed since the last major Ganja earthquake ($M > 7$) (Ismail-Zadeh et al. 2020). Large, old large and thus still detectable landslides in certain areas may have a seismic origin, while smaller ones might have been eroded or removed due to natural or human-induced processes.

The commonly used landslide CFs encompass various aspects: topography, hydrology, geology, land use/cover and man-made features. Topographic factors include slope, aspect, elevation, plan curvature, profile curvature and sediment transport index. Hydrological factors consist of rainfall, solar radiation, stream power index, topographic wetness index (TWI), distance to rivers and river density. Geological factors involve lithology, distance to faults and fault density. Land use/cover (LULC) and normalised difference vegetation index (NDVI), while man-made factors encompass distance to roads and road density (Taloor et al. 2024).

In this study, 16 CFs that are seismicity, lithology, LULC, NDVI, plan curvature, precipitation, profile curvature, slope, soil type, drainage density, elevation, aspect, Topographic Position Index (TPI), Normalized Difference Water Index (NDWI), soil moisture and fault density are utilised and were prepared in ArcGIS Pro and Google Earth Engine (GEE). The data sources, types and spatial resolution for various CFs used in this study are illustrated in Table 1. The primary source for topographic data was the Digital Elevation Model (DEM) by the Shuttle Radar Topography Mission (SRTM) with a

Table 1. Used landslide causative factors for landslide susceptibility mapping with their sources.

Factors	Data sources	Data type	Resolution/Scale
Slope, Aspect, Elevation, TPI, Drainage density, Plan Curvature, Profile Curvature	SRTM, USGS	Raster	27 m
Lithology	Commission of the Geological Map of the World (CGMW)	Vector	1:3 750 000
Soil type	FAO-UNESCO	Vector	1:5.000.000
Seismicity	AIR, GEM, and GEORISK (2018)	Vector	
Fault density	The Active Faults of Eurasia Database (AFEAD)	Vector	1:1,000,000
Precipitation	CHIRPS	Raster	5566 m
LULC	SILVIS LAB	Raster	30 m
NDVI	Landsat 8, USGS	Raster	30 m
NDWI	Landsat 8, USGS	Raster	30 m
Soil moisture	Google and NSIDC	Raster	9000 m

spatial resolution of 30 meters. Using ArcGIS Pro, this data was utilised to generate slope, aspect, elevation, profile curvature, drainage density, TPI and plan curvature.

Furthermore, the drainage density of the region was then derived using the line density tool. Lithology data was obtained from a vector-formatted lithology map provided by the Commission of the Geological Map of the World (CGMW) (Jansen et al. 2010; Gleeson et al. 2011). Soil-type data was acquired from the Digitized Soil Map of the World provided by FAO-UNESCO at a scale of 1:5,000,000. LULC data for the year 2015 was obtained from SILVIS LAB (Buchner et al. 2020) as a 30-meter resolution raster map, Landsat-8 satellite imagery with a 30-meter resolution was acquired from the USGS Earth Explorer and used to calculate the NDVI and NDWI. Seismic activity data from Shen-Tu et al. (2018) was derived in .csv format. This data was converted into point data and then transformed into a raster format using the kernel density tool within ArcGIS Pro.

Additionally, fault data was obtained from the Active Faults of Eurasia Database (AFEAD) (Zelenin et al. 2022) at a scale of 1:500,000. It was converted into fault density by using a line density tool. Yearly precipitation data from 2000 to 2022 was acquired using Google Earth Engine from the Climate Hazards Group InfraRed Precipitation with Station data (CHIRPS) (Funk et al. 2015). The data has a coarse resolution of 5,566 meters. To account for potential temporal variations, the yearly sum for each year was calculated, and the median value across all 22 years was used for analysis. Collecting and processing these diverse datasets will establish a comprehensive understanding of the potential factors influencing LS within the LC-KB. All the dataset prepared in this study have datum WGS 1984 and UTM zone 38 N projection system.

3.3. Methods for multicollinearity analysis

Multicollinearity analysis is employed to evaluate the correlation among various independent factors contributing to landslides. In this analysis, one independent variable can be accurately predicted by other closely connected variables in a regression model (Kab et al. 2023). Statistical measures such as variance inflation factors (VIF), tolerance (TOL) and Pearson correlation coefficients (PCC) are utilised to identify the presence of multicollinearity in our dataset. VIF applies least squares regression and quantifies how much the variance of an estimated regression coefficient increases if predictors are correlated (Naikoo et al. 2023). The TOL value is obtained by taking the reciprocal of the VIF. It represents the proportion of variance in a predictor variable not explained by the other predictor variables.

In this study, the PCC was also utilised to identify the correlation between two predisposing factors of landslides. The PCC was introduced by Karl Pearson (1895). It serves as a widely used approach for quantifying the extent of linear correlation between two variables, X and Y (Wang et al. 2020). In LS analysis, it is crucial to eliminate CFs that exhibit strong correlations (with values exceeding 0.80) to ensure that the chosen factors remain relatively independent (Wang et al. 2020).

3.4. Method for LS modelling

Given the comprehensive nature of the landslide inventory accessible for this study, deterministic methods, including the SVM, LGR and XGBoost, are employed to enhance the comprehensiveness and accuracy of LS results at a regional level. These models were chosen based on an extensive literature review which demonstrated their popularity, interpretability and proven performance in similar studies (Khalil et al. 2022; Sun et al. 2021). While models such as Random Forest (RF) and CNNs are indeed powerful, RF has performance characteristics like XGBoost, and CNN-based approaches generally require spatially structured data such as satellite imagery or DEM windows as input (Mohan et al. 2022). Our input data consisted of extracted point-based features, which align more closely with tabular-based models like XGBoost.

Python was used for modelling, with Scikit-learn implementing SVM, LGR and XGBoost. GridSearchCV, a hyperparameter tuning technique was used to choose optimal modelling parameters. This method systematically searches through a predefined grid of parameter values to identify the combination that yields the best model performance. It evaluates all possible combinations of the specified parameters using cross-validation to ensure robustness and avoid overfitting. Visualization was performed

using Matplotlib and Seaborn for general plotting, while Scikit-plot generated model evaluation metrics such as confusion matrices and ROC curves, enhancing model accuracy and interpretability.

3.4.1. SVM model

The SVM is a supervised ML model tailored for classification and regression tasks. Fundamentally, SVM operates on the principle of separating the hyperplane, maximum hypermargin plane, the soft margin, and the kernel function (Noble 2006): it identifies a line or hyperplane within a higher-dimensional space capable of delineating input data into distinct classes. Introducing a soft margin permits a degree of misclassification or anomalies, fostering enhanced generalisation for linearly inseparable data. It also employs a mathematical function known as a kernel to transform input data into a desired format (Huang and Zhao 2018). The SVM's ultimate output is a probabilistic binary landslide value, denoted as 0 and 1 (Micheletti et al. 2014).

In this study, the RBF kernel function is implemented. Multiple training sessions were performed to have the best hyperparameters for optimal accuracy of the SVM model. This fine-tuning process resulted in the following best parameters: $C = 1$, gamma $= 0.1$, and kernel = RBF. $C = 1$ indicates a balanced trade-off. The gamma value of 0.1 suggests a moderate level of influence, which helps capture complex patterns in the data without overfitting. The RBF kernel is a popular choice for nonlinear data because it can handle complexity by mapping input features into higher-dimensional space, making it suitable for modelling LS (Chen et al. 2016).

3.4.2. LGR model

LGR functions as a multivariate regression, establishing a relationship between the dependent variable, the spatial distribution of existing landslides and a set of independent variables representing various landslide-controlling factors (Brock et al. 2020). The LGR algorithm estimates the probability of landslide occurrence through maximum likelihood estimation. This requires transforming the dependent variable into a logit form (Rai et al. 2022). Consequently, the presence and absence of landslides are coded as 1 and 0, respectively. The LGR equation, which quantifies the relationship between these controlling factors and the observed landslide occurrences in Eq. (1), is as follows.

$$\boldsymbol{f}(\boldsymbol{z}) = \boldsymbol{\pi}\left(\boldsymbol{S} = 1|\boldsymbol{X}_!, \boldsymbol{X}_2, \ldots \boldsymbol{X}_{\boldsymbol{\eta}}\right) = \frac{1}{1 + \boldsymbol{e}^{-(\boldsymbol{\beta}_\circ + \sum_{i=1}^{n} (\boldsymbol{\beta}_I \boldsymbol{X}_i))}} \tag{1}$$

$p(S = 1|X_1, X_2, \ldots, X_n)$ denotes a pixel affected by slope failure, given the presence of independent variables from X_1 to Xn. Here, β_0 represents the constant term of the equation, while $\beta_1, \beta_2, \ldots, \beta_n$ represent the coefficients of the variables $X_1, X_2, \ldots, Xn$. Grid search is used for a hyperparameter tuning that exhaustively searches through a specified parameter grid to find the optimal set of parameters for an LR model. This fine-tuning process resulted in the following best parameters: $C = 0.001$, penalty = L2 and solver = newton-cg. The $C = 0.001$ indicates a high level of regularisation. The 'l2' penalty refers to Ridge regularisation, and it helps manage multicollinearity and prevents the model from fitting the noise in the training data (Sun et al. 2021). Furthermore, the Newton-CG solver uses the Newton-Conjugate Gradient method, suitable for logistic regression with L2 regularisation.

3.4.3. XGBoost model

XGBoost, a scalable ML system for tree boosting developed by Chen and Guestrin (2016), is among the most popular regression algorithms known for its high accuracy. It offers advantages like parallel computation, optimised memory usage and efficient sparse data handling. Compared to linear models, XGBoost often delivers superior prediction accuracy (Zhang et al. 2023). It is an optimised extension of the gradient boosting algorithm, which combines the outputs of weak learners sequentially to enhance performance (Hastie et al. 2009). XGBoost employs numerous classifications, and regression trees and integrates them using the gradient boosting.

It features three key aspects: a regularised objective function for improved generalisation, gradient tree boosting for additive training, and shrinkage and column subsampling to prevent overfitting (Chen and Guestrin 2016). The hyperparameters for the XGBoost were optimised using grid search to achieve

the best performance, resulting in gamma set to 0, learning-rate set to 0.2, max-depth set to 7 and n-estimators set to 100.

The learning-rate helps prevent overfitting by reducing the weight of each step, making the model more robust. The max-depth parameter specifies the maximum depth of a tree. The n-estimator parameter indicating the number of boosting rounds or trees must be balanced; a low value can cause underfitting, while a very high value can significantly increase computation time (Kavzoglu and Teke 2022). These settings provided the optimal balance between model performance and computational efficiency.

3.5. Validation methods

Statistical analysis is mandatory for any LS modelling to validate the reliability of the outcome. Receiver Operative Characteristic (ROC), confusion matrix and other statistical evaluation methods are the most used statistical validation techniques for GIS-based LS mapping. This study uses those statistical evaluation measures to validate the results of the three models. The ROC plot is a model validation technique, which is measured by plotting the True Positive (TP) rate (sensitivity) against the False Positive (FP) rate (1-specificity) with various cut-off thresholds (Zhao and Chen 2020). It primarily focused on assessing binary classification model outcomes; this method delineates classifier performance across varying thresholds, manifested as coordinates on a Cartesian plane with values ranging from 0 to 1 (Chen et al. 2017).

The ROC curve calculates the Area Under the Curve (AUC) value. The AUC obtained from the ROC plot indicates the accuracy of the respective model. A well-performing model produces a value close to 1.0, whereas an inaccurate model gets a value close to 0.5 (Abdelkader and Csámer 2025). This indicator is widely used in studies in different disciplines and has been tested in various precision prediction models. The prediction effect has also been widely recognised.

A confusion matrix is implemented on the testing dataset to assess the performance metrics for landslide and non-landslide classes. These metrics are calculated based on the confusion matrixes resulting from the LGR, SVM and XGBoost models. In the confusion matrix, TP is the number of landslide points correctly classified to the landslide class, and True Negative (TN) is the total number of non-landslide points correctly classified to the non-landslide class. FP is the number of landslide points classified as the non-landslide class; False Negatives (FN) is the non-landslide points.

Furthermore, three different parameters are used to statistically describe the total areas resulting from TP, FP and FN: precision, recall and F1. Precision (P) was used to define how many of the classified areas are landslides (Fang et al. 2020). Recall (R) was used to determine how much of the actual landslide areas were classified in the images (Yu et al. 2021). The well-known F1 measure was additionally used to calculate the balance between the two mentioned accuracy descriptors (Fang et al. 2020).

4. Results

4.1. Landslide inventory mapping

The lack of a landslide inventory in certain regions hinders the creation of LS maps. For this purpose, a comprehensive inventory is developed for the missing region of the lesser Caucasus. Google Earth Pro is utilised to prepare the landslide polygons suitable for fine- and medium-scale landslides due to their image resolution. These landslides were combined with the Matossian and Panek Inventories, accounting for 3,659 landslides altogether. The updated catalogue includes landslide polygons already recorded in previous inventories and the missing landslides in the Lesser Caucasus.

Figure 2 shows the mapped landslides for the landslide inventory in the Lesser Caucasus of Azerbaijan. The spatial distribution of landslides in the inventory map was statistically analysed, showing that the average landslide size is 96,559 m^2. The minimum and maximum surface areas of landslides are 116 m^2, and 25.5 km^2, respectively. The frequency distribution of landslide sizes in each region in Figure 3 shows that the number of occurrences decreases across all regions as the landslide size increases.

Most landslides tend to fall within the smaller area classes (e.g. below 10,000 m^2), which is consistent with the general trend and power-law distribution in landslide inventories where small-scale landslides

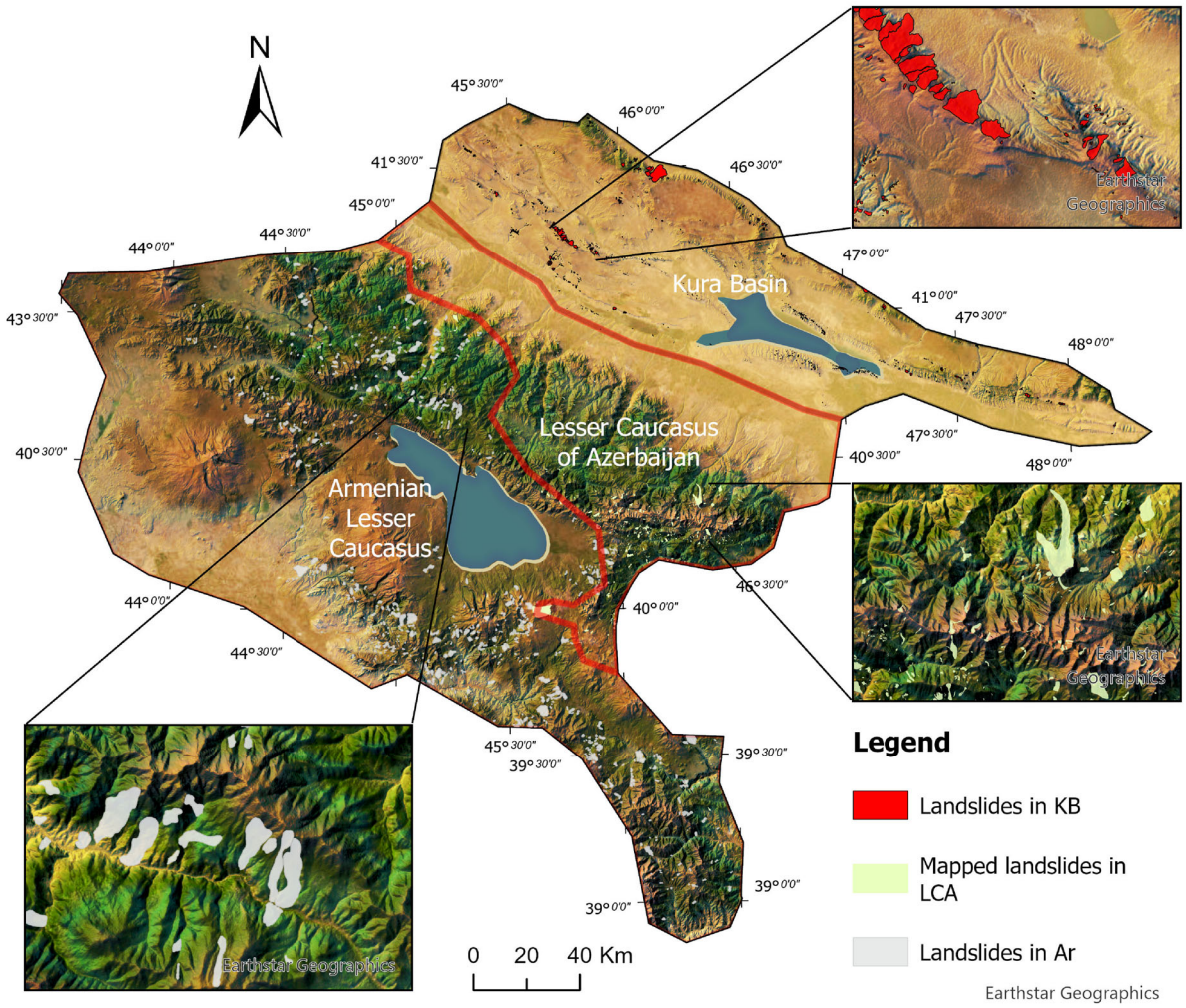

Figure 2. Detailed distribution of three landslide inventories of Kura Basin (KB), Lesser Caucasus of Azerbaijan (LCA) and Armenia (Ar) highlighting the spatial distribution of mapped landslide occurrences.

are more frequent than large-scale landslides. Moreover, the Matossian Armenian inventory has a higher frequency of larger landslides (above 2,000 m^2) than the other two inventories. Furthermore, Kura Basin and Lesser Caucasus of Azerbaijan exhibit a similar trend for more minor landslides but diverge slightly in larger area size classes.

After compiling the three inventories, 3,659 landslides for LC-KB were used in the modelling phase. The landslide events were mapped as polygons, and the boundary of the polygons showed the spatial extents of landslides with both depleted and accumulated zones. Later, the polygons were converted into points that represent the landslides' Scarp. Then, non-landslide points were created in the same number (3,659) as the landslide points.

The non-landslide points were created in the same number as the landslide points in ArcGIS Pro. The non-landslide points were distributed randomly outside the landslide buffer zones in the study area. Afterwards, training, testing and validation datasets were randomly selected among the landslide and non-landslide points to prepare LS models. The inventory data were divided randomly into training, testing, and validation datasets using a 70:15:15 sampling ratio.

4.2. Thematic maps of CFs

The data used for preparing different thematic layers of CFs were derived from several sources. A total of 16 CFs that includes seismicity, lithology, LULC, NDVI, NDWI, soil moisture, plan curvature, precipitation, profile curvature, slope, soil type, drainage density, elevation, aspect, TPI and fault density

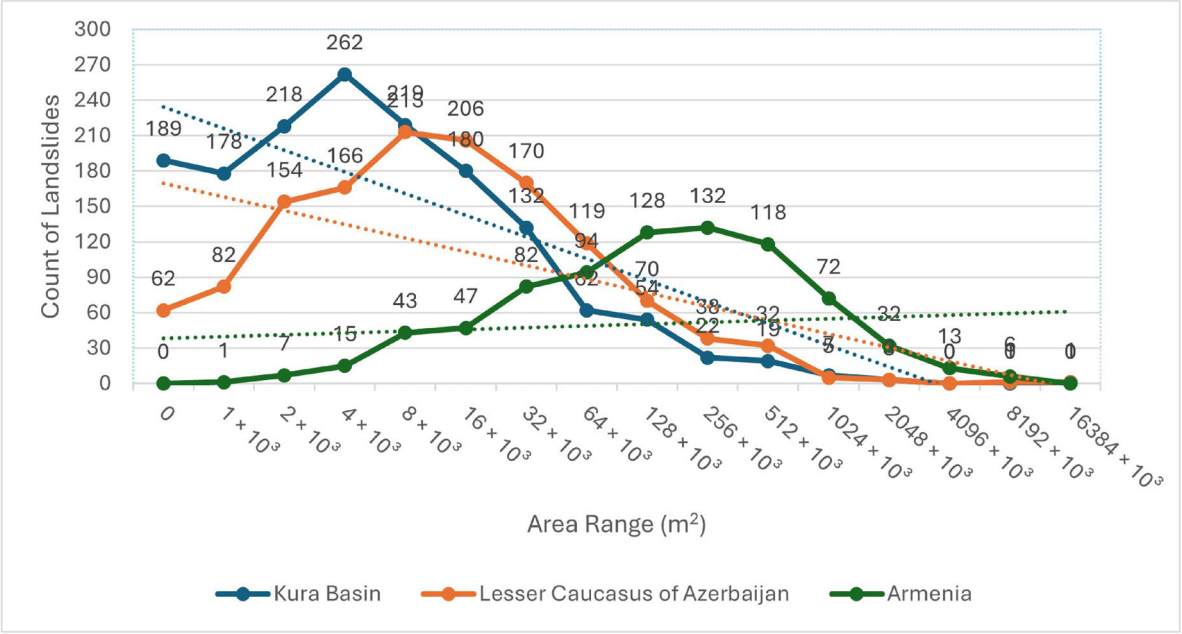

Figure 3. Frequency and size distribution of landslides across three regions (Armenia, Kura Basin, and Lesser Caucasus of Azerbaijan). The *x*-axis represents area size classes (in square meters), while the *y*-axis shows the number of landslides within each class.

were utilised and prepared in ArcGIS Pro and GEE. All the thematic layers of the CFs were normalised and standardised prior to modelling. In each landslide polygon, a point was generated in the top 30% of the polygon based on slope degree using python. This approach, adapted from Pourghasemi et al. (2020), aims to better represent the likely initiation zone of the landslide and improve the spatial accuracy of susceptibility modelling. Using the point shapefile of landslide inventory, values from all causative factors were extracted using extract multi-values to points tool. For clarity, the map of four key CFs is presented in Figure 4, focusing on their direct relevance to the study. Additional CFs map covering the remaining ten factors are provided in the appendix (Figure 1A).

The spatial relationship between the normalised thematic layers (classified into five categories ranging from 1 to 5) and landslide (LS = 1) and non-landslide (LS = 0) points was examined and plotted, as can be seen in Figure 5. These plots reveal how each factor's distribution varies in regions with and without landslides. Notably, the slope emerges as a crucial factor, with a higher density of landslide points observed at steeper slopes. Similarly, seismicity and fault density show significant differences, suggesting that areas with higher seismic activity and fault density are more prone to landslides.

Factors like NDVI and LULC reveal that specific vegetation and land cover types are more susceptible to landslides, while plan and profile curvature, precipitation and drainage density exhibit varying degrees of influence. Aspect shows minor differences, suggesting a limited role in landslide occurrence, while TPI displays notable differences, indicating its importance in identifying landslide-prone areas.

4.3. Multicollinearity among the CFs

In this study, Pearson's correlation coefficients, VIF and TOL, were applied as indicators to detect multicollinearity among the used landslide CFs. This aids in understanding the individual influence of each factor, guiding the selection of variables for more accurate LS models. Table 2 assesses multicollinearity among various CFs influencing LS by listing their TOL and VIF values. Low VIF values, such as seismicity and LULC, and high TOL values, like aspect and plan curvature, indicate low multicollinearity, suggesting these factors do not significantly overlap with others.

Moderate multicollinearity is observed in factors like lithology and NDVI. High multicollinearity is seen in factors such as soil type and elevation. The highest multicollinearity is found in soil moisture

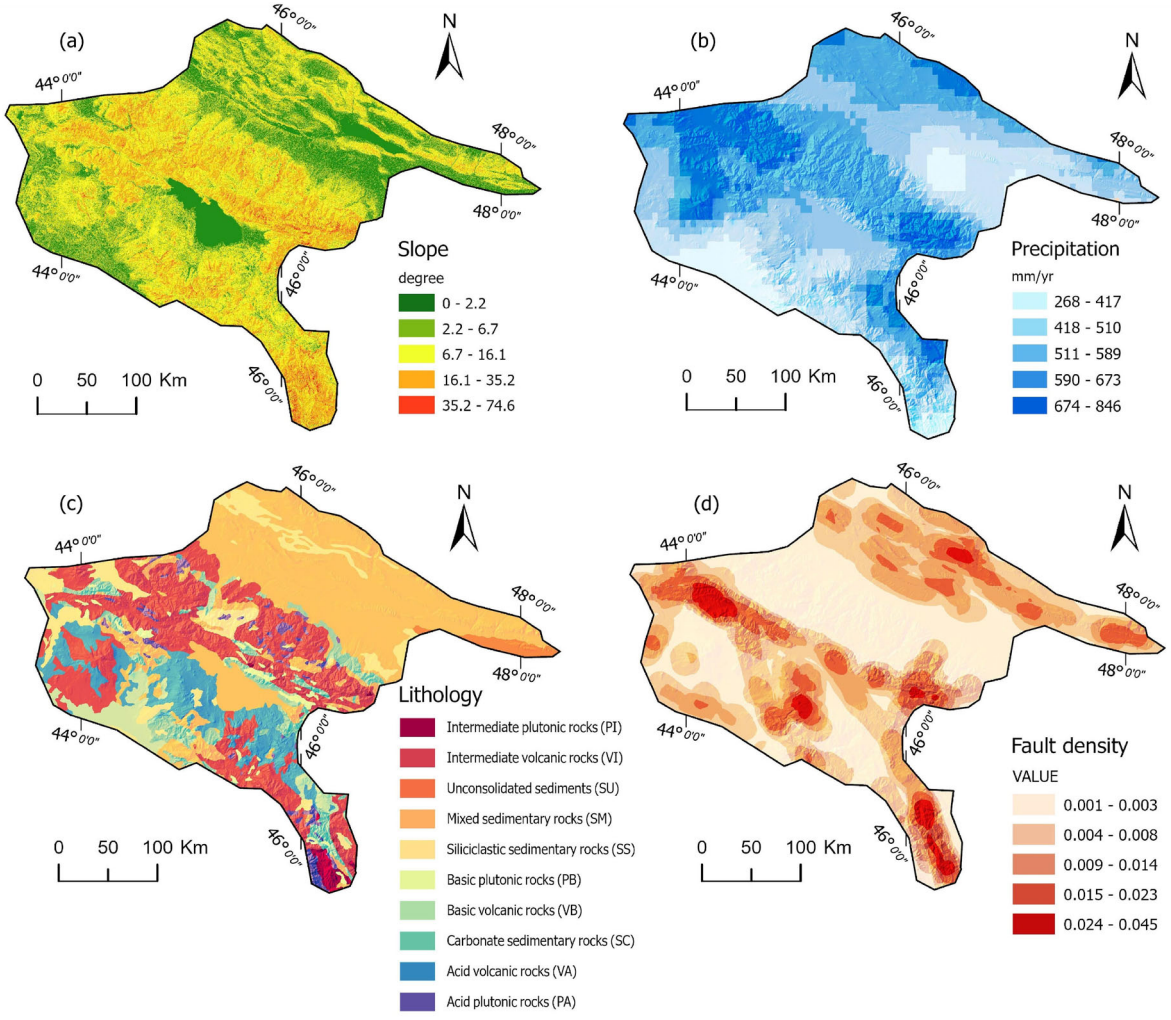

Figure 4. Map of four key landslide CFs used in this study: (a) slope, (b) precipitation, (c) lithology and (d) fault density.

and NDWI, suggesting a significant overlap with other variables and a potential need for dimensionality reduction or variable exclusion to improve model stability and interpretability. Therefore, soil moisture and NDWI were excluded from further analysis.

The heatmap shown in Figure 6 visually represents the correlation coefficients between the used landslide CFs. Dark red signifies strong positive correlations, dark blue indicates strong negative correlations and grey denotes weak or no correlations. For instance, there is a strong positive correlation exists between NDVI and Precipitation, indicating that areas with higher vegetation indices tend to have higher precipitation levels.

Slope, with the highest positive correlation coefficient, is the most significant factor influencing LS, indicating that steeper slopes are strongly associated with a higher likelihood of landslides. Conversely, Aspect (–0.18) and Drainage Density (–0.15) show moderate negative correlations, suggesting that specific orientations and drainage densities contribute less to LS. The soil moisture and NDWI variables that exceeded the pairwise correlation threshold of ±0.75 were removed from the data due to substantial correlation.

4.4. LS maps

The relative importance of various landslide CFs across three ML models, LGR, SVM and XGBoost, is presented in Table 3. Slope consistently emerges as the most significant factor across all models, particularly in XGBoost with the highest importance being at 31. Aspect and seismicity also demonstrate

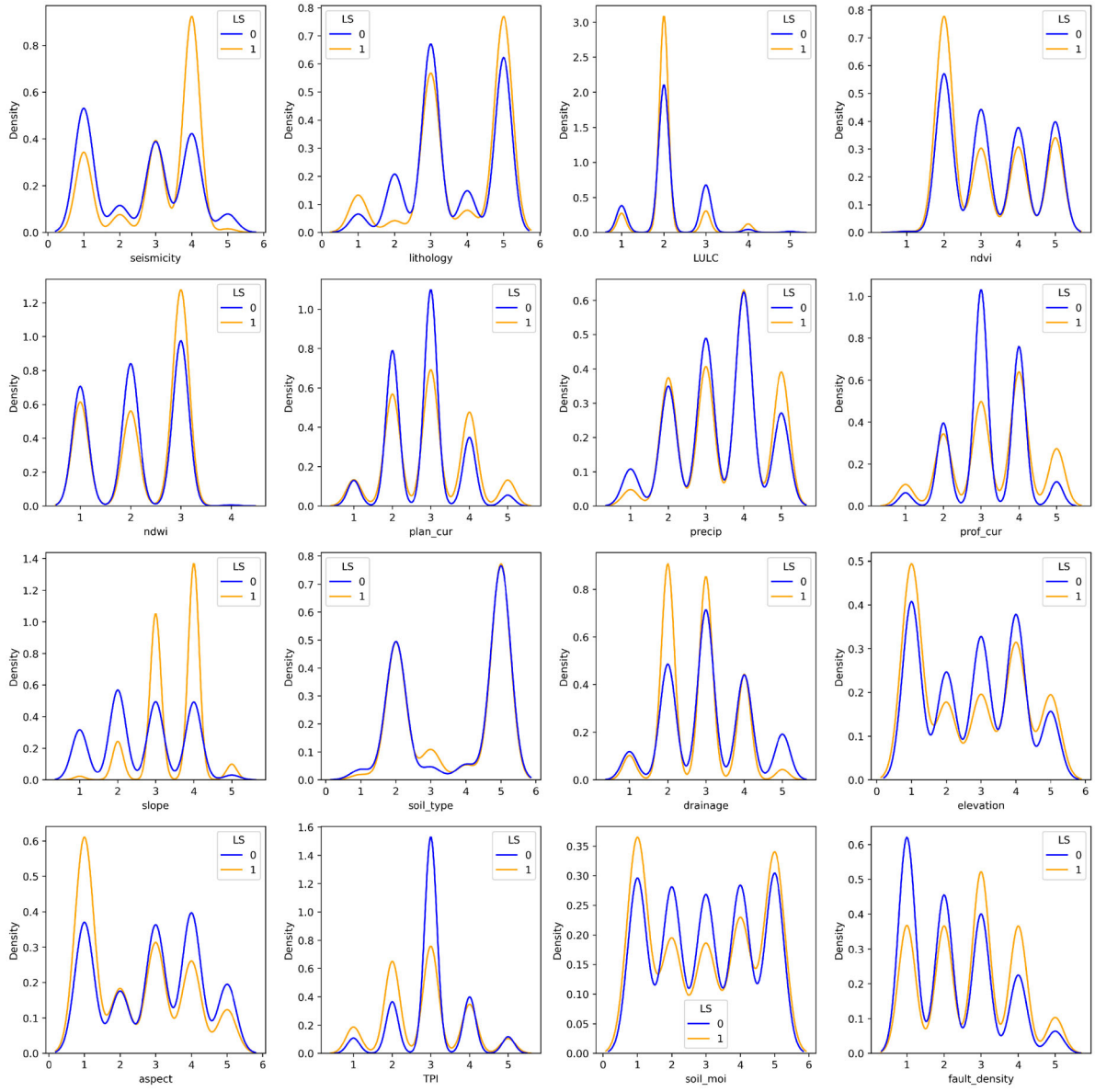

Figure 5. Spatial relationship between landslide inventory and thematic layers (0 = non landslide and 1= landslide).

Table 2. Multicollinearity evaluation of landslide CFs.

Factors	TOL	VIF	Factors	TOL	VIF
Seismicity	0.76	1.31	Soil type	0.37	2.71
Lithology	0.51	1.97	Drainage density	0.77	1.3
LULC	0.83	1.2	Elevation	0.27	4.21
NDVI	0.3	4	Aspect	0.95	1.05
Plan curvature	0.81	1.23	TPI	0.86	1.16
Precipitation	0.73	1.37	Fault density	0.79	1.27
Profile curvature	0.77	1.3	Soil moisture	0.22	4.4
Slope	0.72	1.39	NDWI	0.18	5.58

high importance across all models, with notable scores of 10 in LGR and moderate values in SVM and XGBoost. NDVI and fault density show varied importance, being more critical in LGR and SVM than XGBoost.

Elevation also exhibits varied significance, with greater weight in SVM and XGBoost and less importance in LGR. The TPI and drainage density are moderately important across all models, indicating their consistent influence. Moreover, profile curvature, plan curvature, LULC, drainage density and soil

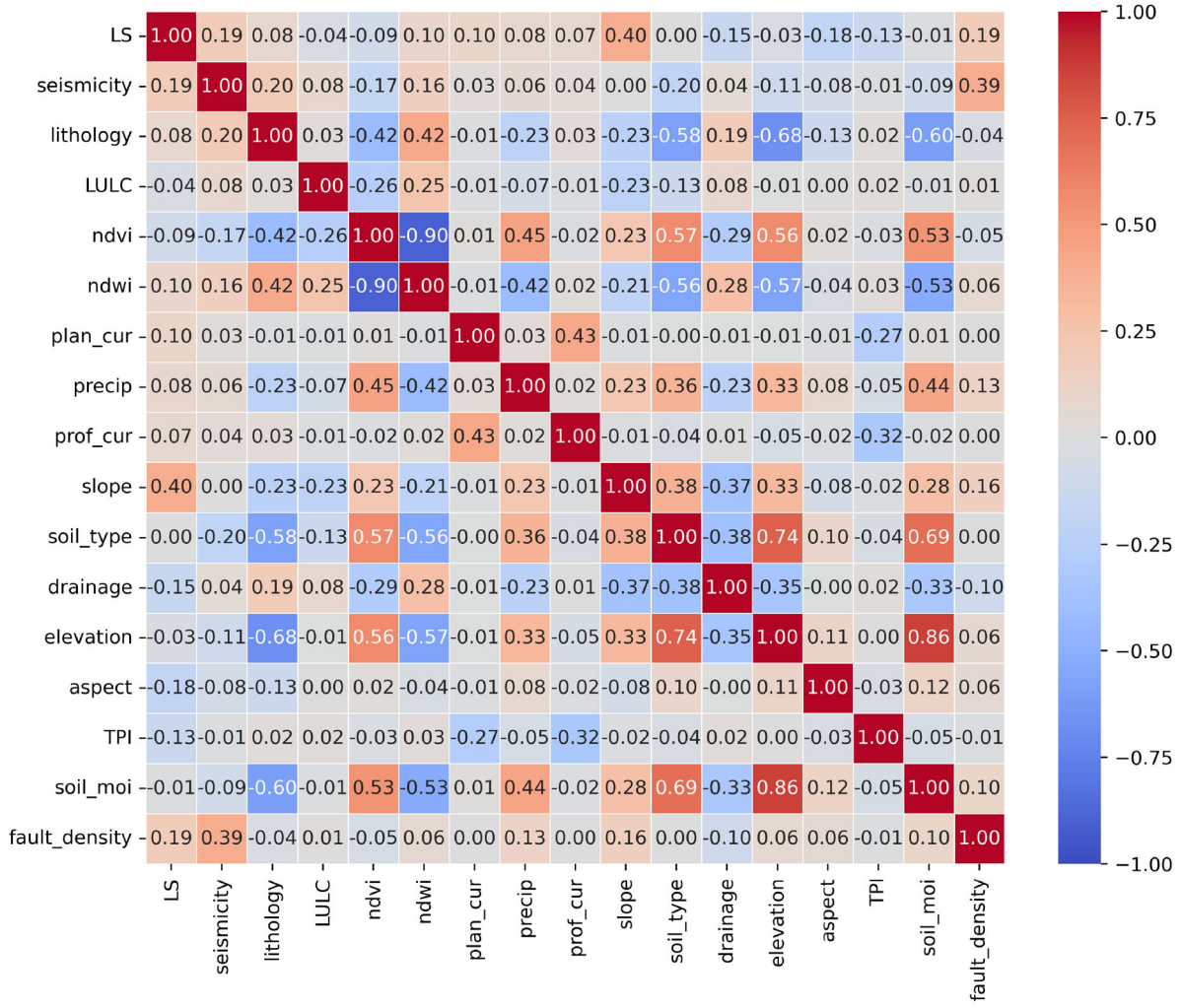

Figure 6. Heat map based on Pearson's correlation coefficient results among causative factors and with respect to landslides.

Table 3. CFs weights from three ML models, with the highest weights highlighted in red and higher weights in bold.

Factors	LGR	SVM	XGBoost	Factors	LGR	SVM	XGBoost
Slope	**18**	**19**	**31**	Plan curvature	5	3	5
Aspect	**10**	4	5	Lithology	**8**	**8**	4
Seismicity	**10**	**9**	**9**	Precipitation	7	**10**	5
NDVI	**9**	4	5	Profile curvature	3	2	3
Fault density	**10**	**8**	4	Elevation	3	**13**	**9**
TPI	**8**	5	7	LULC	1	3	6
Drainage density	7	5	5	Soil type	2	7	4

type have less weight overall. This variation highlights the diverse sensitivities of the models to different factors, emphasising the importance of model selection in LS studies.

The resulting weights of the models for the CFs were used to produce the LS maps in ArcGIS pro using the weighted overlay method. The black dots in the LS maps represent the actual landslide events used to relate the outcomes of the models with the produced landslide inventory. The LS maps were divided into five susceptibility classes: very low (dark green), low (light green), moderate (yellow), high (orange) and very high (red).

The LS map developed using the LGR model is shown in Figure 7(a). The landslide occurrences predominantly align with the high and very high susceptibility areas. These high susceptibility zones are mainly located in the central and southern parts of the region and correspond to steep slopes and areas with significant fault densities. The northern and some eastern regions, marked by dark and light green,

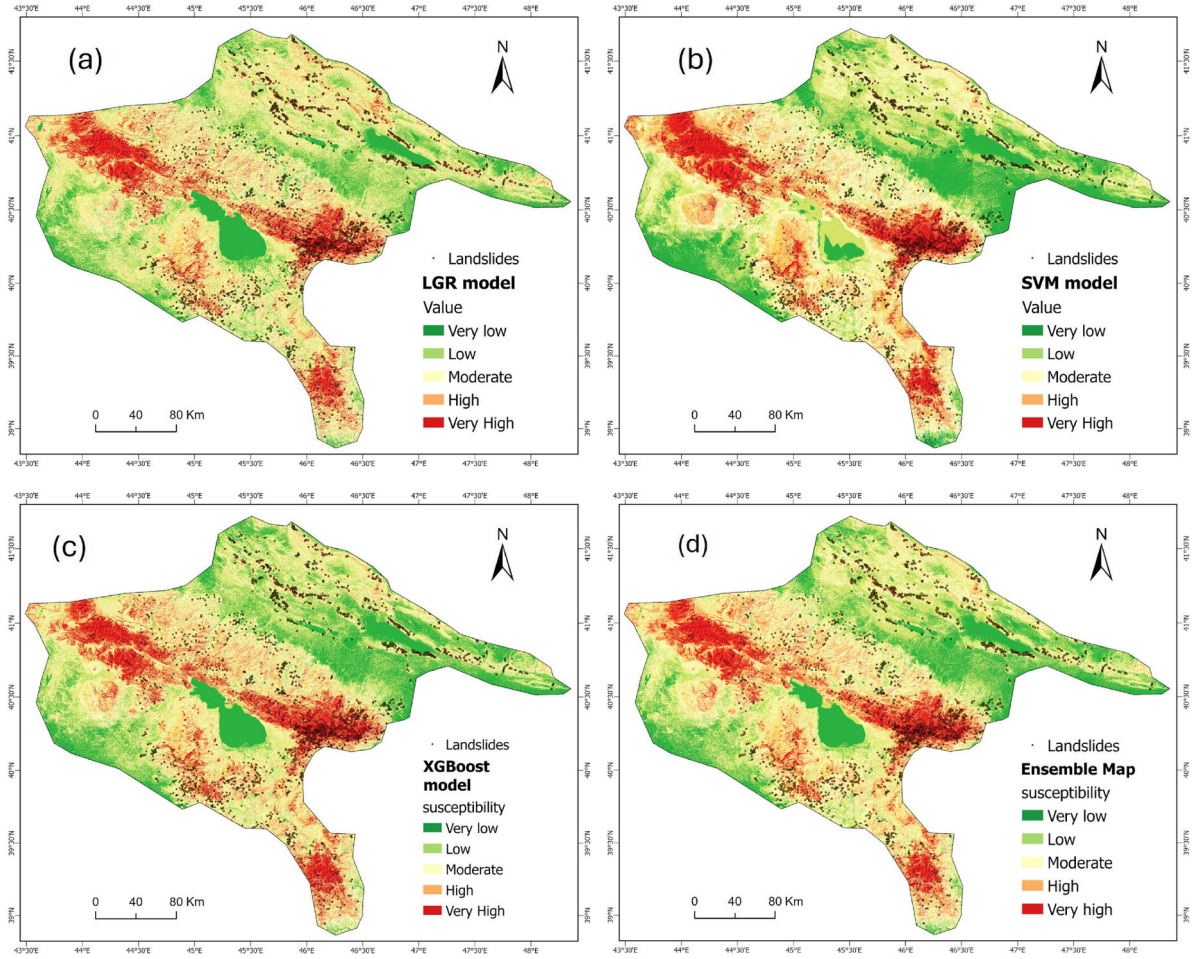

Figure 7. LS maps generated using different models with (a) LGR, (b) SVM, (c) XGBoost and (d) Ensemble map. Landslide inventory points are overlaid for validation, illustrating the spatial distribution of predicted susceptibility across the study area.

indicate very low susceptibility zones, suggesting more stable terrain and less likely to experience landslides.

Furthermore, the LS map generated using the SVM model for the study region is shown in Figure 7(b). The high likelihood of landslides is primarily concentrated in the central and southwestern regions, which are characterised by steep slopes and significant fault densities. Conversely, the green areas, denoting very low and low susceptibility, are predominantly located in the northern and eastern parts of the region, indicating stable terrains less prone to landslides.

Additionally, the LS map in Figure 7(c) illustrates susceptibility in the region using the XGBoost model. Areas with very high and high susceptibility are predominantly located in the central and southeastern parts of the region, indicated by red and orange. Conversely, regions shaded in green and light green, mainly found in the northern and northwestern parts, show very low susceptibility, suggesting a lower likelihood of landslides. Clustering these dots in the high and very high susceptibility zones demonstrates the model's accuracy in identifying potential landslide-prone areas.

For each model, the area and percentage of the total area are provided for each susceptibility class, as shown in Figure 7. LGR identifies the most significant area under Moderate susceptibility (29%), followed by Low (26%) and High (22%), with Very Low and Very High classes occupying the least area (14% and 9%, respectively). The SVM model also predicts the largest area under Moderate susceptibility (26%) but with slightly more areas classified as Very Low (18%) compared to LGR.

The High Susceptibility class covers 21% of the area, with Very High at 10%, as seen in Figure 8. The XGBoost model shows a similar trend, with the Moderate class covering 25% of the area and slightly higher percentages for Very Low (18%) and Very High (10%) classes than SVM and LR.

Figure 8. Histogram of landslide susceptibility classes, as determined by the LGR, SVM and XGBoost models.

Among the three models, XGBOOST predicts the smallest area under Low susceptibility (25%). XGBoost also tends to predict a more even distribution across the classes, whereas LGR and SVM show a stronger focus on the Moderate susceptibility class.

An ensemble map combining the susceptibility of the XGBoost, SVM and LGR models is presented in Figure 7(d). In ArcGIS Pro, the sum of the values from the three-susceptibility rasters was used to create a new ensemble map representing the combined susceptibility. The ensemble map demonstrates a balanced distribution of susceptibility classes, with 16% of the area classified as Very Low, 26% as Low, 27% as Moderate, 21% as High and 10% as Very High. This distribution suggests that the ensemble map effectively illustrates the range of LS within the study area. The spatial distribution of LS areas is classified into same five categories (Very Low, Low, Moderate, High and Very High), as in the LS maps by the ML models: LGR, SVM and XGBoost.

4.5. Validation of models

The ROC curves for the LGR, SVM, and XGBoost models shown in Figure 9 illustrate the model's performance distinguishing between landslide and non-landslide-prone areas. The AUC values for both training and validation datasets are provided for each model. The LGR model achieves an AUC of 0.81 for training and 0.78 for validation, indicating moderate performance. The SVM model performs better, with an AUC of 0.94 for training and 0.87 for validation, demonstrating its superior ability to generalise from the training data. The XGBoost model outperforms both, with an AUC of 0.97 for training and 0.89 for validation, indicating the highest predictive accuracy and robustness among the three models.

The confusion matrices for the evaluation of the used models, LGR, SVM and XGBoost distribution of TN, FN, FP and TP, along with their corresponding percentages is also carried out. The LGR model shows 412 TN (37.52%), 135 FP (12.30%), 162 FN (14.75%) and 389 TP (35.43%). The SVM model indicates improved performance with 452 TN (41.17%), 95 FP (8.65%), 122 FN (11.11%) and 429 TP (39.07%). The XGBoost model further enhances performance with 451 TN (41.07%), 96 FP (8.74%), 115 FN (10.47%) and 436 TP (39.71%).

These results demonstrate that both SVM and XGBoost outperform LR in minimising FP and FN. The performance comparison of the three ML models for LSM on the testing dataset as illustrated in Table 4 reveals that XGBoost outperforms the other models in all evaluated metrics. Specifically,

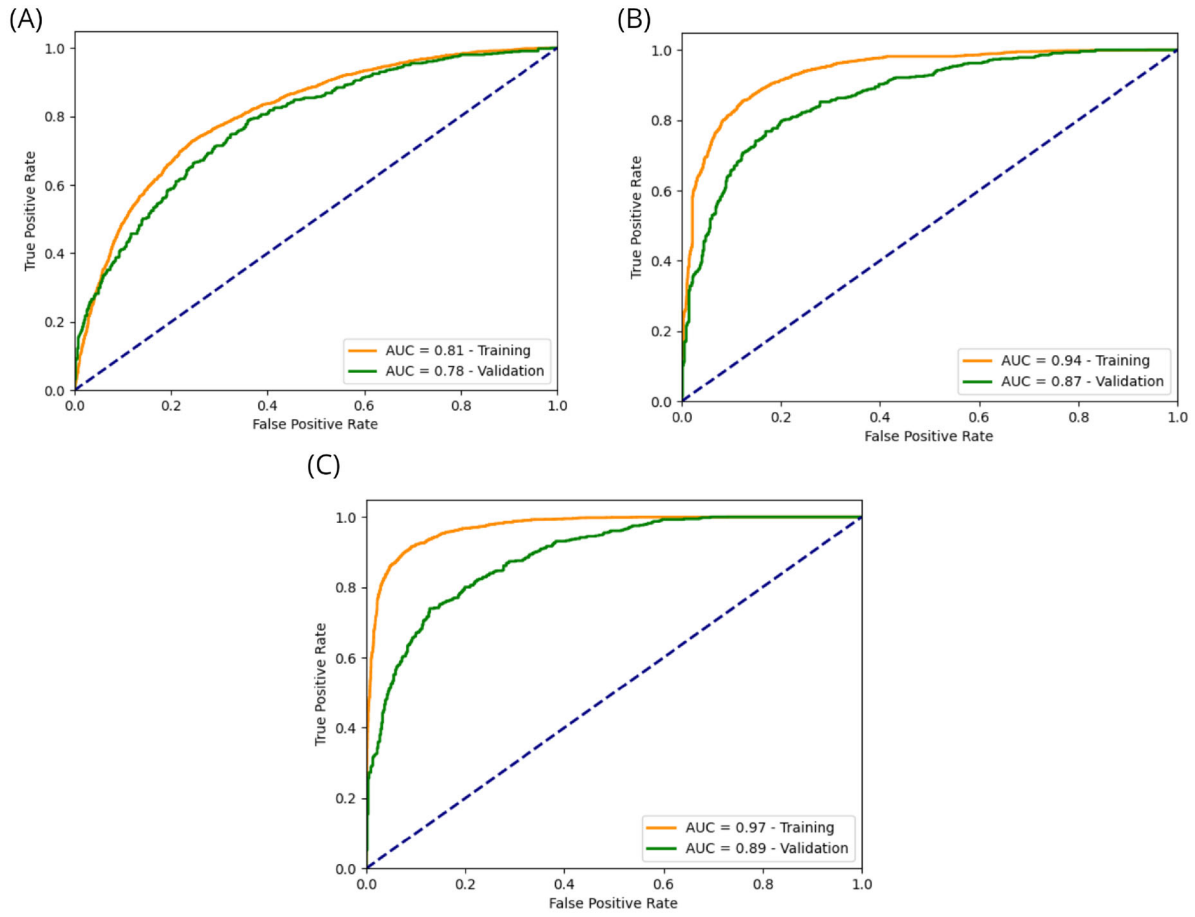

Figure 9. Percent area of under-the-curve (AUC) values for landslide susceptibility maps using (A) LGR, (B) SVM and (C) XGBoost models.

Table 4. Performance of different models on the testing data set.

	LGR	SVM	XGBoost
Precision	0.74	0.82	0.82
Recall	0.71	0.78	0.79
F1-score	0.72	0.80	0.81
Accuracy	0.73	0.80	0.81

XGBoost achieves the highest precision, recall, F1-score and accuracy, indicating its superior ability to accurately and comprehensively identify landslide-prone areas.

SVM also performs well making it a strong alternative. LR, while still effective, shows lower precision, recall, F1-score, and accuracy compared to SVM and XGBoost, suggesting that it is less reliable in predicting LS. Overall, the results indicate that XGBoost is the most effective model for accurate landslide prediction, followed closely by SVM, with LGR being the least effective among the three.

5. Discussion

This research centres on a region with a fold-and-thrust belt and intricate climate, geomorphology, tectonics, geography and geology. The Caucasus Mountains exhibit a distinctive characteristic: diverse climate across short distances. This phenomenon is also reflected in changes in the vegetation patterns (Nakhutsrishvili and Abdaladze 2017). Due to the diverse heterogeneities in this area, natural hazards, particularly landslides, are likely to occur frequently. As shown in the Figure 1, the study area map includes major faults, devastating earthquakes, volcanoes, lakes and rivers complementing the hydrological and geophysical description of the area.

Robust modelling of LS presents a significant challenge, necessitating the creation of a comprehensive landslide inventory, selecting suitable CFs, and appropriate modelling and validation methods. For the landslide inventory, the compiled landslide polygons of LC-KB used in this study outline the whole landslide depleted and accumulated zones. The Matossian and current inventory documented the landslides resulting from the gravitational mass movements. However, at higher altitudes (>2,800 m), distinguishing gravitational mass movements from glacial erosion and deposition in the Lesser Caucasus presents a significant challenge in landslide demarcation.

Another challenge is the presence of dense forests, which makes it difficult to demarcate and map landslides. As a result, landslide inventories may miss a significant number of landslides, especially in heavily forested regions. The Matossian inventory used in this study for the western Armenian Lesser Caucasus likely underestimates the number of landslides in those regions, marked by the highest LS, notably due to factors like the steeper slopes, high seismicity and humidity. The dense forest cover is likely the main reason for this region's limited number of mapped landslides.

No consensus exists on which factors should be selected to identify landslide CFs. Therefore, various techniques, such as multicollinearity tests, have been employed to identify relationships among landslide indicators that could adversely affect model accuracy. These tests are carried out to ensure that no correlation exists among the selected factors. The VIF, TOL and PCC analyses of CFs revealed high multicollinearity for soil moisture and NDWI, leading to their exclusion from further analysis.

The correlation coefficient of CFs with landslides indicates that slope, seismicity and fault density are the most critical factors, with a higher occurrence of actual mapped landslides. A strong correlation was found between seismic factors and landslide occurrences, such as seismicity and fault density. These similar correlation patterns were also observed by Pánek et al. (2024) and Matossian et al. (2020).

In contrast, a weak correlation was observed between climatic factors and landslide occurrences, such as NDWI, soil moisture and drainage density. However, precipitation does have a slightly positive correlation. These correlation results contradict the findings of the Japan International Cooperation Agency (JICA), Georisk CJSC (2006) study, which states that precipitation is the primary cause of landslide occurrences in the Lesser Caucasus, while the effects of earthquakes and active faults are minimal.

The seismic effect is also evident from the Spitak and Ganja earthquakes, where small and large landslides occurred in the vicinity of the respective epicentres. Pánek et al. (2024) found a correlation between landslides and faults in the Kura basin, noting that more than 50% of the total landslide area is situated within one kilometre of thrust faults. The mapping of faults in Azerbaijan's Lesser Caucasus is likely incomplete, resulting in missing faults that were not recorded, which is also highlighted by Matossian et al. (2020).

Furthermore, for drainage density, the initial expectation was that areas with high drainage density would be more prone to landslides due to increased moisture content. This is because wet soil loses strength and becomes looser, making it more susceptible to failure. However, this study revealed the opposite pattern. Areas with the most landslides have the lowest drainage density.

In contrast, regions with fewer landslides have the highest drainage density, likely due to the presence of many non-perennial streams densely distributed across the nearly flat landscapes. Additionally, older landscapes due to prolonged incision and erosion tend to be more stable with well-developed drainage systems. It also helps remove excess water making the slopes less prone to landslides compared to younger, poorly developed landscapes.

All the models assign the highest weight to slope, followed by seismicity, elevation, precipitation, lithology and fault density, which are the important factors for LS in the study area. The SVM model shows that elevation and slope have a significant influence. The susceptibility maps show that the LS is comparatively high in the LC-KB region's central, western and southeastern sections. In contrast, most northern regions have very low to moderate LS. This is possible due to the northern region's gentle slope, low precipitation and low elevation variation, similar conclusions were drawn by Pánek et al. (2024).

Further, a central region has high LS because, in this part, the terrain is mostly hilly with a very high elevation, precipitation and steep slopes. Conducting a LS study on a regional scale with diverse terrain can be challenging. By applying a generalised model to the entire region, the results with high susceptibility in the central part are prominent as compared to the northern low elevated and gentle slope areas.

However, a focused study on just the northern part would reveal different results that are otherwise overlooked in the broader analysis. Additionally, when the regional susceptibility maps are displayed for a specific, focused area, there may be large discrepancies with the actual situation. Regional landslide inventories may also face similar challenges.

Additionally, the observed discrepancies in susceptibility emphasise the importance of considering multiple models when assessing LS. The LGR model appears to designate the north as a higher susceptibility zone than SVM and XGBoost, which shows that the LGR model's estimated results closely match the ground truth. In contrast, the SVM and XGBoost models reflect an underestimation of susceptibility.

However, the LGR model shows mostly moderate susceptibility in the low-elevated and gentle slope region of the Kura Basin, indicating a potential overestimation of susceptibility and sensitivity of the LR model in the basin regions. Conversely, the centre-south and central regions exhibit a lower susceptibility on the LR map than on the SVM map. This generalisation effect of LS by the LGR model leads to higher FN responses, leading to lower statistical performance. XGBoost generally shows lower susceptibility in the north compared to LGR and SVM. The XGBoost and SVM models are more suitable for outlining focusing effects as landslide concentrations more influence them in mountainous terrain.

The differences in model performance can be attributed to their underlying architecture, learning algorithms and ability to capture feature interactions. XGBoost utilises an ensemble of decision trees known for their inherent ability to capture nonlinear relationships and feature interactions. This likely explains its superior performance in capturing the interplay of factors influencing landslides. It also employs a forward stage-wise approach, where each tree split directly improves the model's performance. This allows XGBoost to identify the most impactful features and their interactions efficiently.

While the SVM model can handle nonlinear relationships through kernels, interpreting the importance of features in the transformed space can be challenging. Its performance may decline in regions with high spatial variability and overlapping feature distributions. This might explain why SVM results, while more accurate than LGR, fell short of XGBoost's performance. The LGR model assumes a linear relationship between features and the outcome. This inherent limitation restricts its ability to capture complex interactions, potentially explaining the lower accuracy and higher FN rate compared to XGBoost and SVM.

LGR optimises the log-likelihood function and feature importance derived from the estimated linear coefficients. This method assumes features act independently, potentially overlooking crucial interactions that influence LS. The result shows that most of the study area falls under low and moderate susceptibility zones. Selecting a single model for delineating susceptibility could lead to underestimation or overestimation of susceptibility. Furthermore, to avoid potential spatial overfitting due to the proximity of landslide points, the landslide inventory was prepared by applying a spatial filtering process to reduce clustering of nearby events, thereby minimising spatial bias. Furthermore, the grid search technique was implemented with a spatial cross-validation strategy, namely k-fold, to ensure that model training and validation were spatially independent (Dahim et al. 2023).

Therefore, combining LGR, SVM and XGBoost maps into the ensemble susceptibility map shows improved results with a balanced distribution of susceptibility classes, addressing a key limitation observed in individual models. This distribution suggests the ensemble map effectively captures the entire spectrum of LS within the LC-KB.

For ROC-AUC scores across all models evaluated, there is a consistent trend where higher AUC scores are achieved on the training data. This phenomenon suggests that the models benefit from the larger dataset during training, allowing models to learn different patterns effectively. Among the models, XGBoost emerges as the top performer with the highest AUC scores on both training and validation sets. In contrast, LGR and SVM also exhibit strong performances but show a greater disparity between their training and validation AUC scores, suggesting potential overfitting to the training data.

After fine-tuning, the confusion matrix shows better performance by all three models. The difference between precision and recall scores is significantly lower for XGBoost, followed by SVM and LGR, due to the optimisation of hyperparameters. The high F1 score further indicates a good balance between these two metrics. The higher accuracy also signifies that the models accurately classified landslide and non-landslide areas in the study area.

Notably, the model performance varies across different terrains due to heterogeneity in geomorphological, geological and environmental conditions. In this study, while some variability in performance across terrain types is there, the final LS maps align well with the historical landslide inventory, indicating that the models were able to generalize effectively across the study area. Additionally, it is important to note that the different CFs can differ across terrains and may have varying degrees of importance depending on the local topography and geomorphic context. This spatial variability in CF influence can inherently affect model performance (Bounab et al. 2022). Nevertheless, the overall consistency between the LS maps and known landslide occurrences supports the reliability and robustness of the results of this study.

The performance of the models also suggests that nonlinear XGBoost and SVM models are superior to the linear LGR model. It shows how hyperparameter optimisation strategies affect models' accuracy and predictive performance. These findings underscore the critical role of validation in assessing model performance realistically. While models may excel in training data due to their learning capacity, their ability to generalise to new data is crucial for practical applications. Therefore, effective validation strategies are essential to ensure that models maintain high performance across diverse datasets, enhancing their reliability and utility in real-world scenarios.

6. Conclusion

This study presents a comprehensive landslide inventory, with analyses of CFs and modelling of LS on a regional level for the LC-KB. First a comprehensive landslide inventory for the Lesser Caucasus of Azerbaijan with 1,322 landslides was established. Subsequently, this inventory was integrated with existing landslide inventories from the Kura Basin and Armenian Lesser Caucasus, resulting in a regional inventory encompassing 3,659 landslides. A total of 16 CFs were prepared initially, and the statistical relationship between them and landslides was studied using the inventory map. Multicollinearity tests, including VIF, TOL and PCC analysis, revealed a high degree of multicollinearity between soil moisture and NDWI. To ensure the robustness of the model and avoid biased results, these factors were excluded from further analysis.

Moreover, three data mining models, namely LGR, SVM and XGBoost, were used to produce the first regional-level ensemble LS map for the LC-KB. The models were fine-tuned using a grid search technique to identify the optimal parameters. The model results and spatial analysis of CFs indicate that slope and seismic factors have a stronger influence on landslide occurrences in the study area. All the models show promising results, with XGBoost models having 81% accuracy, followed by SVM and LGR with 80% and 73% accuracy, respectively, on the testing dataset. To avoid under and over estimation, the ensemble susceptibility map is derived by combining the XGBoost, SVM and LGR LS maps. The ensemble map shows a balanced distribution across various susceptibility classes. This suggests a more comprehensive spatial coverage of the LS within the LC-KB. The results of this study can aid in landslide management by enhancing the understanding of key input parameters influencing LS. It can guide targeted management interventions, such as controlling LS or mitigating the impact of landslides.

Recommendations

Based on the results of this research, we recommend using the LGR model for LS assessment over mixed mountain and basin regions, such as in the Caucasus, due to its stronger generalisation capabilities. In contrast, the XGBoost and SVM models are better suited for local scale analysis because of localised focusing effects, particularly in mountainous areas.

Limitations and future work

This study offers significant scientific insights into LS analysis, though there are limitations that future research should address. First, classifying landslides into different types and developing susceptibility maps for each type are necessary. Additionally, expanding field surveys for landslide locations will enhance the accuracy of predictions, and utilising high-resolution images could significantly improve

the results. Furthermore, dense forest cover and high elevations in the study area may have led to underrepresentation of landslides, especially in remote sensing-derived inventories. This limitation could introduce bias in susceptibility results. While difficult to quantify without ground-truth data, it should be considered when interpreting the findings. Despite these limitations, the findings can assist stakeholders in choosing the best models and identifying the most sensitive and uncertain parameters to develop robust management plans.

Disclosure statement

The authors declare no competing financial or personal interests that could have influenced the work presented in this research. The study was conducted independently, without any direct commercial or institutional influence that could create a conflict of interest. Furthermore, any institutional affiliations mentioned in this article are solely for academic and research purposes. All data providers and relevant contributions are acknowledged in the manuscript.

Author contributions

CRediT: **Israr Ullah**: Conceptualization, Data curation, Formal analysis, Validation, Writing – original draft; **Klaus Reicherter**: Supervision, Writing – review & editing; **Tomáš Pánek**: Writing – review & editing; **Alessandro Tibaldi**: Writing – review & editing; **Husam Al-Najjar**: Project administration, Supervision, Validation, Visualization, Writing – review & editing; **Bahareh Kalantar**: Funding acquisition, Investigation, Validation, Visualization, Writing – review & editing; **Naonori Ueda**: Funding acquisition, Writing – review & editing; **Hans-Balder Havenith**: Writing – review & editing.

ORCID

Bahareh Kalantar http://orcid.org/0000-0002-2822-3463

Data availability statement

Data will be accessible upon request to the first author.

References

Abdelkader MM, Csámer Á. 2025. Comparative assessment of machine learning models for landslide susceptibility mapping: a focus on validation and accuracy. Nat Hazards. 121(9):10299–10321. doi: 10.1007/s11069-025-07197-0.

Adamia S, Alania V, Chabukiani A, Chichua G, Enukidze O, Sadradze N. 2010. Evolution of the Late Cenozoic basins of Georgia (SW Caucasus): a review. SP. 340(1):239–259. doi: 10.1144/SP340.11.

Akgun A. 2012. A comparison of landslide susceptibility maps produced by logistic regression, multi-criteria decision, and likelihood ratio methods: a case study at İzmir, Turkey. Landslides. 9(1):93–106. doi: 10.1007/s10346-011-0283-7.

Alcaraz Tarragüel A, Krol B, van Westen C. 2012. Analysing the possible impact of landslides and avalanches on cultural heritage in Upper Svaneti, Georgia. J Cult Herit. 13(4):453–461. doi: 10.1016/j.culher.2012.01.012.

Aslam B, Zafar A, Khalil U. 2021. Development of integrated deep learning and machine learning algorithm for the assessment of landslide hazard potential. Soft Computing. 25(21):13493–13512. doi: 10.1007/s00500-021-06105-5.

Avagyan A, Sosson M, Sahakyan L, Sheremet Y, Vardanyan S, Martirosyan M, Muller C. 2018. Tectonic evolution of the Northern margin of the Cenozoic Ararat basin, Lesser Caucasus, Armenia. Journal of Petroleum Geology. 41(4):495–511. doi: 10.1111/jpg.12718.

Avagyan A, Sosson M, Philip H, Karakhanian A, Rolland Y, Melkonyan R, Rebaï S, Davtyan V. 2005. Neogene to Quaternary stress field evolution in Lesser Caucasus and adjacent regions using fault kinematics analysis and volcanic cluster data. Geodinamica Acta. 18(6):401–416. doi: 10.3166/ga.18.401-416.

Bounab A, Agharroud K, El Kharim Y, El Hamdouni R, Faghloumi L. 2022. The importance of investigating causative factors and training data selection for accurate landslide susceptibility assessment: the case of Ain Lahcen commune (Tetouan, Northern Morocco). Geocarto International. 37(25):9967–9997. doi: 10.1080/10106049.2022.2028905.

Boynagryan V. 2009. Landslides in Armenia. Rev. Roum. Géogr. 53(2):197–208.

Brock J, Schratz P, Petschko H, Muenchow J, Micu M, Brenning A. 2020. The performance of landslide susceptibility models critically depends on the quality of digital elevation models. Geomatics Nat Hazards Risk. 11(1): 1075–1092. doi: 10.1080/19475705.2020.1776403.

Buchner J, Yin H, Frantz D, Kuemmerle T, Askerov E, Bakuradze T, Bleyhl B, Elizbarashvili N, Komarova A, Lewińska KE, et al. 2020. Land-cover change in the Caucasus Mountains since 1987 based on the topographic correction of multi-temporal Landsat composites. Remote Sensing Environment. 248:111967. doi: 10.1016/j.rse.2020.111967.

Chen T, Guestrin C. 2016. XGBoost: a scalable tree boosting system. In: *Proceedings of the 22nd ACM SIGKDD International Conference on Knowledge Discovery and Data Mining*; 2016 Aug 13–17; San Francisco, CA, USA. New York (NY): Association for Computing Machinery. p. 785–794. doi: 10.1145/2939672.2939785

Chen W, Chai H, Zhao Z, Wang Q, Hong H. 2016. Landslide susceptibility mapping based on GIS and support vector machine models for the Qianyang County, China. Environmental Earth Sciences. 75(6):1–13. doi: 10.1007/s12665-015-5093-0.

Chen W, Pourghasemi HR, Panahi M, Kornejady A, Wang J, Xie X, Cao S. 2017. Spatial prediction of landslide susceptibility using an adaptive neuro-fuzzy inference system combined with frequency ratio, generalized additive model, and support vector machine techniques. Geomorphology. 297:69–85. doi: 10.1016/j.geomorph.2017.09.007.

Conforti M, Robustelli G, Muto F, Critelli S. 2012. Application and validation of bivariate GIS-based landslide susceptibility assessment for the Vitravo river catchment (Calabria, south Italy). Natural Hazards. 61(1):127–141. doi: 10.1007/s11069-011-9781-0.

Dahim M, Alqadhi S, Mallick J. 2023. Enhancing landslide management with hyper-tuned machine learning and deep learning models: predicting susceptibility and analyzing sensitivity and uncertainty. Frontiers in Ecology and Evolution. 11:1–22. doi: 10.3389/fevo.2023.1108924.

Fang Z, Wang Y, Peng L, Hong H. 2020. Integration of convolutional neural network and conventional machine learning classifiers for landslide susceptibility mapping. Computers & Geosciences. 139:104470. doi: 10.1016/j.cageo.2020.104470.

Fomenko IK, Zerkal OV, Strom A, Shubina D, Musaeva L. 2021. The Krasnogorsk Landslide (Northern Caucasus): its evolution and modern activity. In: understanding and reducing landslide disaster risk: volume 5 catastrophic landslides and frontiers of landslide science. Cham (Switzerland): Springer Int Publ. p. 49–56.

Forte AM, Cowgill E, Bernardin T, Kreylos O, Hamann B. 2010. Late Cenozoic deformation of the Kura fold-thrust belt, southern Greater Caucasus. Bull Geol Soc Am. 122(3-4):465–486. doi: 10.1130/B26464.1.

Forte AM, Cowgill E, Murtuzayev I, Kangarli T, Stoica M. 2013. Structural geometries and magnitude of shortening in the eastern Kura fold-thrust belt, Azerbaijan: implications for the development of the Greater Caucasus Mountains. Tectonics. 32(3):688–717. doi: 10.1002/tect.20032.

Forte AM, Sumner DY, Cowgill E, Stoica M, Murtuzayev I, Kangarli T, Elashvili M, Godoladze T, Javakhishvili Z. 2015. Late Miocene to Pliocene stratigraphy of the Kura Basin, a subbasin of the South Caspian Basin: implications for the diachroneity of stage boundaries. Basin Research. 27(3):247–271.

Funk C, Peterson P, Landsfeld M, Pedreros D, Verdin J, Shukla S, Husak G, Rowland J, Harrison L, Hoell A, et al. 2015. The climate hazards infrared precipitation with stations—a new environmental record for monitoring extremes. Science Data. 2(1):150066. doi: 10.1038/sdata.2015.66.

Gaprindashvili G, Van Westen CJ. 2016. Generation of a national landslide hazard and risk map for the country of Georgia. Natural Hazards. 80(1):69–101. doi: 10.1007/s11069-015-1958-5.

Gleeson T, Smith L, Moosdorf N, Hartmann J, Dürr HH, Manning AH, van Beek LPH, Jellinek AM. 2011. Mapping permeability over the surface of the Earth. Geophysical Research Letters. 38(2):n/a–n/a. doi: 10.1029/2010GL045565.

Guzzetti F, Reichenbach P, Ardizzone F, Cardinali M, Galli M. 2006. Estimating the quality of landslide susceptibility models. Geomorphology. 81(1-2):166–184. doi: 10.1016/j.geomorph.2006.04.007.

Hassangavyar MB, Samani AN, Rashidi S, Tiefenbacher JP. 2020. Catchment-scale soil conservation: using climate, vegetation, and topo-hydrological parameters to support decision making and implementation. Sci Total Environ. 712:136124. Amsterdam (Netherlands): Elsevier. doi: 10.1016/j.scitotenv.2019.136124.

Hastie T, Tibshirani R, Friedman J. 2009. Boosting and additive trees. In: *The elements of statistical learning: data mining, inference, and prediction*. New York (NY): Springer. p. 337–387.

Havenith HB, Guerrier K, Schlögel R, Braun A, Ulysse S, Mreyen AS, Victor KH, Saint-Fleur N, Cauchie L, Boisson D, et al. 2022. Earthquake-induced landslides in Haiti: analysis of seismotectonic and possible climatic influences. Natural Hazards and Earth System Sciences. 22(10):3361–3384. doi: 10.5194/nhess-22-3361-2022.

Hoogendoorn RM, Boels JF, Kroonenberg SB, Simmons MD, Aliyeva E, Babazadeh AD, Huseynov D. 2005. Development of the Kura delta, Azerbaijan; a record of Holocene Caspian sea-level changes. Marine Geology. 222-223:359–380. doi: 10.1016/j.margeo.2005.06.007.

Huang Y, Zhao L. 2018. Review on landslide susceptibility mapping using support vector machines. Catena. 165: 520–529. doi: 10.1016/j.catena.2018.03.003.

Huang F, Xiong H, Jiang SH, Yao C, Fan X, Catani F, Chang Z, Zhou X, Huang J, Liu K. 2024. Modelling landslide susceptibility prediction: a review and construction of semi-supervised imbalanced theory. Earth-Science Review. 250:104700. doi: 10.1016/j.earscirev.2024.104700.

Ismail-Zadeh A, Adamia S, Chabukiani A, Chelidze T, Cloetingh S, Floyd M, Gorshkov A, Gvishiani A, Ismail-Zadeh T, Kaban MK, et al. 2020. Geodynamics, seismicity, and seismic hazards of the Caucasus. Earth-Science Review. 207:103222. doi: 10.1016/j.earscirev.2020.103222.

Jansen N, Hartmann J, Lauerwald R, Dürr HH, Kempe S, Loos S, Middelkoop H. 2010. Dissolved silica mobilization in the conterminous USA. Chemical Geology. 270(1-4):90–109. doi: 10.1016/j.chemgeo.2009.11.008.

Japan International Cooperation Agency (JICA), Georisk CJSC (Armenia). 2006. Joint project: the study on landslide disaster management in the Republic of Armenia; inventory database creation. Yerevan (Armenia): JICA. 68 p. [accessed 2024 Mar 8]. Available from: http://open_jicareport.jica.go.jp/pdf/11834660.pdf.

Justice TE. 2021. Evaluation of manual and semi-automated deep-seated landslide inventory processes: willapa Hills, Washington [dissertation]. Portland (OR): Portland State University. doi: 10.15760/etd.7555.

Kab A, Djerbal L, Bahar R. 2023. Implementation of PCA multicollinearity method to landslide susceptibility assessment: the study case of Kabylia region. Arabian Journal of Geoscience. 16(4):291. doi: 10.1007/s12517-023-11374-5.

Karakhanian AS, Djrbashian RT, Trifonov VG, Philip H, Ritz JF, Giardini D, Balassanian S. 1997. Active faults and strong earthquakes of the Armenian upland. In: Giardini D, Balassanian S, editors. Historical and prehistorical earthquakes in the Caucasus. Dordrecht (Netherlands): Kluwer Academic Publishing. p. 181–187.

Kavzoglu T, Colkesen I, Sahin EK. 2019. Machine learning techniques in landslide susceptibility mapping: a survey and a case study. In: Landslides: theory, Practice and Modelling. Cham (Switzerland): Springer International Publishing. p. 283–301.

Kavzoglu T, Teke A. 2022. Advanced hyperparameter optimization for improved spatial prediction of shallow landslides using extreme gradient boosting (XGBoost). Bulletin of Engineering Geology and the Environment. 81(5):201. doi: 10.1007/s10064-022-02708-w.

Khalil U, Iqra I, Aslam B, Ullah I, Tariq A, Qin S. 2022. Comparative analysis of machine learning and multicriteria decision making techniques for landslide susceptibility mapping of Muzaffarabad district. Frontiers in Environmental Science. 10:1–19. doi: 10.3389/fenvs.2022.1028373.

KoçyIğIt A, Ünay E, Saraç G. 2000. Episodic graben formation and extensional neotectonic regime in west Central Anatolia and the Isparta Angle: a case study in the Aksehir-Afyon Graben, Turkey. SP. 173(1):405–421. doi: 10.1144/GSL.SP.2000.173.01.19.

Kothyari GC, Malik K, Dumka RK, Naik SP, Biswas R, Taloor AK, Luirei K, Joshi N, Kandregula RS. 2022. Identification of active deformation zone associated with the 28th April 2021 Assam earthquake (Mw 6.4) using the PSInSAR time series. Journal of Applied Geophysics. 206:104811. doi: 10.1016/j.jappgeo.2022.104811.

Kumar V, Cauchie L, Mreyen A-S, Micu M, Havenith H-B. 2021. Evaluating landslide response in a seismic and rainfall regime: a case study from the SE Carpathians, Romania. Natural Hazards and Earth System Sciences. 21(12):3767–3788. doi: 10.5194/nhess-21-3767-2021.

Ledworowska A, Braun A, Hovius H-B, Fuchs TM. 2020. 2020. Landslide susceptibility mapping on the country scale with data mining techniques in Armenia. GeoUtrecht. doi: 10.48380/dggv-j9h5-t469. https://www.dggv.de/e-publikationen/landslide-susceptibility-mapping-on-the-country-scale-with-data-mining-techniques-in-armenia/#pll_switcher

Matossian AO, Baghdasaryan H, Avagyan A, Igityan H, Gevorgyan M, Havenith H-B. 2020. A new landslide inventory for the Armenian Lesser Caucasus: slope failure morphologies and seismotectonic influences on large landslides. Geosciences. 10(3):111. doi: 10.3390/geosciences10030111.

McKenzie D. 1972. Active tectonics of the Mediterranean region. Geophysical Journal International. 30(2):109–185. doi: 10.1111/j.1365-246X.1972.tb02351.x.

Micheletti N, Foresti L, Robert S, Leuenberger M, Pedrazzini A, Jaboyedoff M, Kanevski M. 2014. Machine learning feature selection methods for landslide susceptibility mapping. Math Geoscience. 46(1):33–57. doi: 10.1007/s11004-013-9511-0.

Mohan A, Dwivedi R, Kumar B. 2022. Image restoration of landslide photographs using SRCNN. In: Dhawan A, Tripathi VS, Arya KV, Naik K, editors. Recent trends in electronics and communication. VCAS 2020. Lecture Notes in Electrical Engineering. Vol. 777. Singapore: Springer. doi: 10.1007/978-981-16-2761-3_108

Naikoo, Mohd Waseem, Rihan, Mohd, Peer, Arshid Hussain, Talukdar, Swapan, Mallick, Javed, Ishtiaq, Mohammad, Rahman, Atiqur, Shahfahad,. 2023. Analysis of peri-urban land use/land cover change and its drivers using geospatial techniques and geographically weighted regression. Environmental Science and Pollution Research International. 30(55):116421–116439. doi: 10.1007/s11356-022-18853-4.

Nakhutsrishvili G, Abdaladze O. 2017. Vegetation of the Central Great Caucasus along WE and NS transects. In: Nakhutsrishvili G, Abdaladze O, Batsatsashvili K, Spehn E, Körner C, editors. Plant diversity in the Central Great Caucasus: a quantitative assessment. Geobotany Studies. Cham (Switzerland): Springer. doi: 10.1007/978-3-319-55777-9_2.

Nalivkin VD. 1976. Dynamics of the development of the Russian platform structures. In Developments in geotectonics. Vol. 12. Amsterdam (Netherlands): Elsevier. p. 247–262.

Noble WS. 2006. What is a support vector machine? Nature Biotechnology. 24(12):1565–1567. doi: 10.1038/nbt1206-1565.
Pánek T, Březný M, Havenith H-B, Tibaldi A. 2024. Landslides and growing folds: a lesson from the Kura fold-and-thrust belt (Azerbaijan, Georgia). Geomorphology. 449:109059. doi: 10.1016/j.geomorph.2024.109059.
Pearson K. 1895. Correlation coefficient. R Soc Proc. 58:214.
Philip H, Cisternas A, Gvishiani A, Gorshkov A. 1989. The Caucasus: an actual example of the initial stages of continental collision. Tectonophysics. 161(1-2):1–21. doi: 10.1016/0040-1951(89)90297-7.
Pourghasemi HR, Moradi HR, Fatemi Aghda SM. 2013. Landslide susceptibility mapping by binary logistic regression, analytical hierarchy process, and statistical index models and assessment of their performances. Natural Hazards. 69(1):749–779. doi: 10.1007/s11069-013-0728-5.
Pourghasemi HR, Kornejady A, Kerle N, Shabani F. 2020. Investigating the effects of different landslide positioning techniques, landslide partitioning approaches, and presence-absence balances on landslide susceptibility mapping. CATENA. 187:104364. doi: 10.1016/j.catena.2019.104364.
Rai DK, Xiong D, Zhao W, Zhao D, Zhang B, Dahal NM, Wu Y, Baig MA. 2022. An investigation of landslide susceptibility using logistic regression and statistical index methods in Dailekh District, Nepal. Chin Geogr Sci. 32(5):834–851. doi: 10.1007/s11769-022-1304-2.
Saha S, Saha A, Roy B, Sarkar R, Bhardwaj D, Kundu B. 2022. Integrating the Particle Swarm Optimization (PSO) with machine learning methods for improving the accuracy of the landslide susceptibility model. Earth Science Informatics. 15(4):2637–2662. doi: 10.1007/s12145-022-00878-5.
Samia J, Temme A, Bregt A, Wallinga J, Guzzetti F, Ardizzone F, Rossi M. 2017. Do landslides follow landslides? Insights in path dependency from a multi-temporal landslide inventory. Landslides. 14(2):547–558. doi: 10.1007/s10346-016-0739-x.
Santangelo M, Marchesini I, Bucci F, Cardinali M, Fiorucci F, Guzzetti F. 2015. An approach to reduce mapping errors in the production of landslide inventory maps. Natural Hazards and Earth System Science. 15(9):2111–2126. doi: 10.5194/nhess-15-2111-2015.
Shebalin NV, Tatevossian RE. 1997. Catalogue of strong earthquakes ($M \geq 6.0$) for the Global Seismic Hazard Assessment Program test area 'CAUCASUS. In: Historical and Prehistorical Earthquakes in the Caucasus. NATO Meeting; 1997. p. 1–21.
Shen-Tu B, Klein E, Mahdyiar M, Karakhanyan A, Pagani M, Weatherill G, Gee R. 2018. Seismic hazard analysis for Armenia and its surrounding areas. In: *Proceedings of the 16th European Conference on Earthquake Engineering*; 2018 Jun 18–21; Thessaloniki, Greece. A collaboration between AIR Worldwide, GEM, and Georisk.
Sim KB, Lee ML, Wong SY. 2022. A review of landslide acceptable risk and tolerable risk. Geoenvironment Disasters. 9(1):3. doi: 10.1186/s40677-022-00205-6.
Sun D, Xu J, Wen H, Wang D. 2021. Assessment of landslide susceptibility mapping based on Bayesian hyperparameter optimization: A comparison between logistic regression and random forest. Engineering Geology. 281:105972. doi: 10.1016/j.enggeo.2020.105972.
Taloor AK, Abraham A, Parsad G. 2024. Landslide susceptibility modelling in the Doda Kishtwar Ramban (DKR) region of Jammu and Kashmir using Remote Sensing and Geographic Information System. Quaternary Science Advances. 14:100189. doi: 10.1016/j.qsa.2024.100189.
Telesca L, Chelidze T. 2018. Visibility graph analysis of seismicity around Enguri high arch dam, Caucasus. Bulletin of the Seismological Society of America. 108(5B):3141–3147. doi: 10.1785/0120170370.
Tibaldi A, Bonali FL, Mariotto FP, Oppizzi P, Tsereteli N, Havenith H, Babayev G, Pánek T. 2024. Structural expression of the frontal thrust of an active fold-and-thrust belt: the Holocene 123-km-long Kur fault, Greater Caucasus, Azerbaijan. Journal of Structural Geology. 180:105085. doi: 10.1016/j.jsg.2024.105085.
Tsereteli E, Gaprindashvili G, Gaprindashvili M, Bolashvili N, Gongadze M. 2019. 2018. Hazard risk of debris/mud flow events in Georgia and methodological approaches for management. In: Shakoor A, Cato K, editors. IAEG/AEG Annu Meet Proc, Vol 5, p. 153–160. San Francisco, California: Springer International Publishing.
Urushadze TF, Ghambashidze G. 2013. Soils of Georgia. In Soil resources of mediterranean and Caucasus countries. Luxembourg: Publications Office of the European Union. p. 78.
Velayudham J, Kannaujiya S, Sarkar T, Champati Ray PK, Taloor AK, Bisht MPS, Chawla S, Pal SK. 2021. Comprehensive study on evaluation of Kaliasaur landslide attributes in Garhwal Himalaya by the execution of geospatial, geotechnical and geophysical methods. Quaternary Science Advances. 3:100025. doi: 10.1016/j.qsa.2021.100025.
Wallemacq P, Below R, McClean D. 2018. Economic losses, poverty & disasters: 1998–2017. Geneva (CH): United Nations Office for Disaster Risk Reduction. p. 29.
Wang Q, Wang Y, Niu R, Peng L. 2017. Integration of information theory, K-means cluster analysis and the logistic regression model for landslide susceptibility mapping in the Three Gorges Area, China. Remote Sensing. 9(9):938. doi: 10.3390/rs9090938.
Wang Y, Feng L, Li S, Ren F, Du Q. 2020. A hybrid model considering spatial heterogeneity for landslide susceptibility mapping in Zhejiang Province, China. Catena. 188:104425. doi: 10.1016/j.catena.2019.104425.

Xu Z, Che A, Zhou H. 2024. Seismic landslide susceptibility assessment using principal component analysis and support vector machine. Scientific Reports. 14(1):3734. doi: 10.1038/s41598-023-48196-0.
Yetirmishli GJ, Islamova SK, Kazimova SE, Ismailova SS. 2018. Seismic geodynamics of Mingachevir water reservoir. Byulleten Orenburgskogo Nauch Nauk Tsentra URO RAN. 4:12.
Yu X, Zhang K, Song Y, Jiang W, Zhou J. 2021. Study on landslide susceptibility mapping based on rock–soil characteristic factors. Sci Rep. 11(1):15476. doi: 10.1038/s41598-021-9496-5.
Zelenin E, Bachmanov D, Garipova S, Trifonov V, Kozhurin A. 2022. The Active Faults of Eurasia Database (AFEAD): the ontology and design behind the continental-scale dataset. Earth System Science Data. 14(10): 4489–4503. doi: 10.5194/essd-14-4489-2022.
Zhang J, Ma X, Zhang J, Sun D, Zhou X, Mi C, Wen H. 2023. Insights into geospatial heterogeneity of landslide susceptibility based on the SHAP-XGBoost model. Journal of Environment Management. 332:117357. doi: 10.1016/j.jenvman.2023.117357.
Zhao X, Chen W. 2020. Optimization of computational intelligence models for landslide susceptibility evaluation. Remote Sensing. 12(14):2180. doi: 10.3390/rs12142180.
Zhou S, Bondell H, Tordesillas A, Rubinstein BIP, Bailey J. 2020. Early identification of an impending rockslide location via a spatially-aided gaussian mixture model. The Annals of Applied Statistics. 14(2):977–992. doi: 10.1214/20-AOAS1326.

Appendix

Table A1. Spatial relationship and ratings for each causative factor with respect to landslides.

Factors	Class	Class pixels	Class pixels (%)	LS pixels	LS pixels (%)	Rating
NDVI	−0.54–0.019	2,576,027	4	1,066	0	5
	0.02–0.173	20,439,781	30	158,535	19	4
	0.174–0.284	15,358,742	23	190,367	23	3
	0.285–0.395	14,035,147	21	215,188	26	2
	0.396–0.689	14,660,063	22	252,997	31	1
LULC	Deciduous forest	6,595,696	10	112,656	14	5
	Water	2,476,042	4	387	0	5
	Rangeland	42,415,962	63	588,589	72	4
	Cropland	13,289,794	20	84,770	10	3
	Barren	994,293	1	22,396	3	2
	Wetlands	394,206	1	643	0	1
	Built-up	145,319	0	289	0	1
	Mixed forest	288,234	0	3,223	0	1
	Coniferous forest	467,495	1	5,172	1	1
Elevation	−2–550	18,017,652	27	59,684	7	1
	550–1,166	10,883,565	16	102,660	13	2
	1,166–1,785	13,616,916	20	187,846	23	3
	1,785–2,409	16,858,574	25	301,232	37	4
	2,409–4,040	7,693,096	11	166,760	20	5
Profile curvature	−17.21–−0.594	2,129,548	3	34,948	4	3
	−0.593–−0.188	10,642,224	16	161,532	20	2
	−0.187–0.082	30,241,310	45	280,505	34	1
	0.083–0.487	20,509,587	31	271,803	33	4
	0.488–17.239	3,547,134	5	69,394	8	5
Plan curvature	−13.526–−0.653	1,750,690	3	28,758	4	2
	−0.652–−0.237	9,188,093	14	154,608	19	3
	−0.236–0.074	32,193,269	48	316,914	39	4
	0.075–0.489	20,261,622	30	265,010	32	1
	0.49–12.947	3,676,129	5	52,892	6	5
	Total	67,069,803	100	818,182	100	
Slope	0.001–2.215	13,399,044	20	12,651	2	1
	2.216–6.762	18,556,581	28	102,872	13	2
	6.763–16.101	17,030,111	25	353,428	43	3
	16.102–35.279	16,996,166	25	328,105	40	4
	35.28–74.662	1,045,079	2	20,888	3	5
TPI	−158.639–−35.835	2,993,832	4	48,725	6	1
	−35.834–−11.274	8,978,519	13	229,261	28	2
	−11.273–8.953	41,747,647	62	355,144	43	3
	8.954–34.959	9,844,623	15	150,832	18	4
	34.96–209.775	3,564,249	5	34,237	4	5
Precipitation	267–416	4,705,282	7	28,889	4	1
	416–510	12,900,383	19	189,443	23	2
	510–589	18,377,512	27	171,202	21	3
	589–673	21,057,841	31	243,388	30	4
	673–845	10,013,371	15	185,253	23	5

(*continued*)

Table A1. Continued.

Factors	Class	Class pixels	Class pixels (%)	LS pixels	LS pixels (%)	Rating
Fault density	0.001–0.003	23,317,128	35	335,611	41	1
	0.004–0.008	17,155,506	26	180,012	22	2
	0.009–0.014	16,673,955	25	191,807	23	3
	0.015–0.023	7,820,664	12	87,484	11	4
	0.024–0.045	2,102,550	3	23,268	3	5
Aspect	−0.99–25.88	7,687,428	11	85,162	10	3
	25.88–64.09	7,339,998	11	112,816	14	5
	64.09–103.72	7,066,844	11	78,558	10	3
	103.72–140.51	6,656,961	10	60,489	7	1
	140.51–175.89	6,257,294	9	60,236	7	1
	175.89–211.27	7,100,326	11	65,468	8	2
	211.27–248.07	6,947,408	10	74,904	9	2
	248.07–284.86	6,117,421	9	83,755	10	3
	284.86–323.07	6,086,330	9	92,134	11	4
	323.07–359.87	5,766,971	9	104,422	13	4
Seismicity	0.001–0.045	23,686,779	35	353,537	43	1
	0.046–0.054	4,790,672	7	64,792	8	2
	0.055–0.099	16,747,764	25	185,218	23	3
	0.1–0.326	18,570,715	28	202,525	25	4
	0.327–1.471	3,273,873	5	12,110	1	5
Soil type	Chromic Cambisols	3,006,454	4	47,475	6	3
	Haplic Kastanozerns	12,766,318	19	59,342	7	4
	Luvic Chernozems	1,103,824	2	2,425	0	1
	Lithosols	35,106,905	52	671,698	82	5
	Gleyic Solonchaks	534,444	1	0	0	1
	Haplic Xerosols	2,434,201	4	20,808	3	2
	Luvic Xerosols	9,853,107	15	16,385	2	1
	Calcic Xerosols	617,673	1	62	0	1
	Water	1,649,001	2	0	0	1
Lithology	Intermediate plutonic rocks (PI)	662,146	1	6,316	1	1
	Intermediate volcanic rocks (VI)	18,268,533	27	323,187	40	5
	Unconsolidated sediments (SU)	944,620	1	296	0	1
	Mixed sedimentary rocks (SM)	24,621,656	37	213,505	26	5
	Siliciclastic sedimentary rocks (SS)	5,523,969	8	67,897	8	3
	Basic plutonic rocks (PB)	1,038,714	2	18,417	2	2
	Basic volcanic rocks (VB)	2,693,671	4	14,165	2	2
	Carbonate sedimentary rocks (SC)	4,610,400	7	115,996	14	4
	Acid volcanic rocks (VA)	7,013,922	10	46,258	6	3
	Acid plutonic rocks (PA)	1,692,157	3	12,148	1	1
Drainage density	0.001–0.515	6,406,623	10	46,488	5	4
	0.516–0.963	18,437,523	27	403,551	42	3
	0.964–1.278	21,973,679	33	375,894	39	5
	1.279–1.64	14,036,435	21	107,657	11	1
	1.641–2.432	6,215,571	9	19,135	2	2

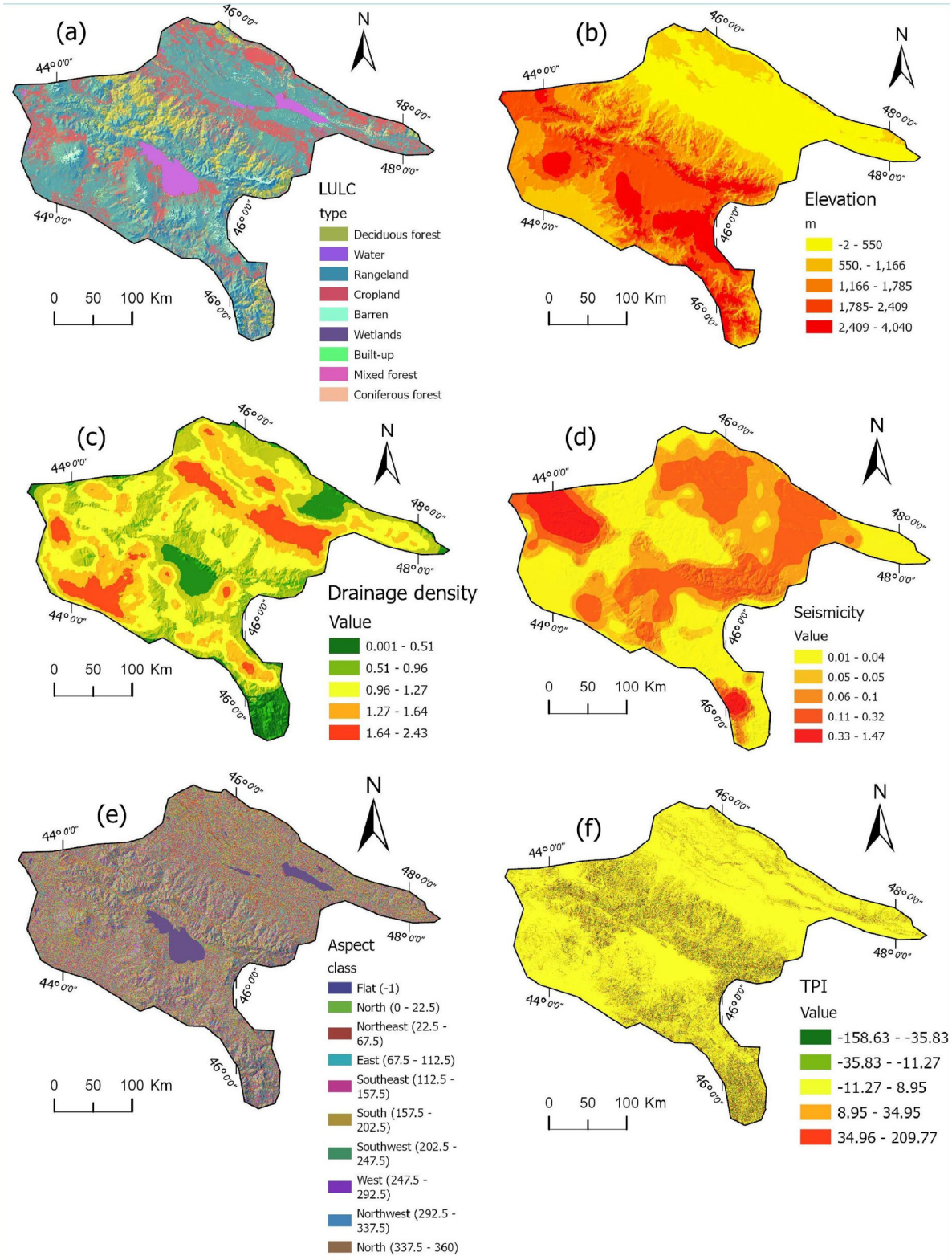

Figure 1A. Landslide causative factor maps used in this study: (a) LULC, (b) Elevation, (c) Drainage density, (d) Seismicity, (e) Aspect, (f) TPI, (g) Plan Curvature, (h) NDVI, (i) Soil type, and (j) Profile Curvature.

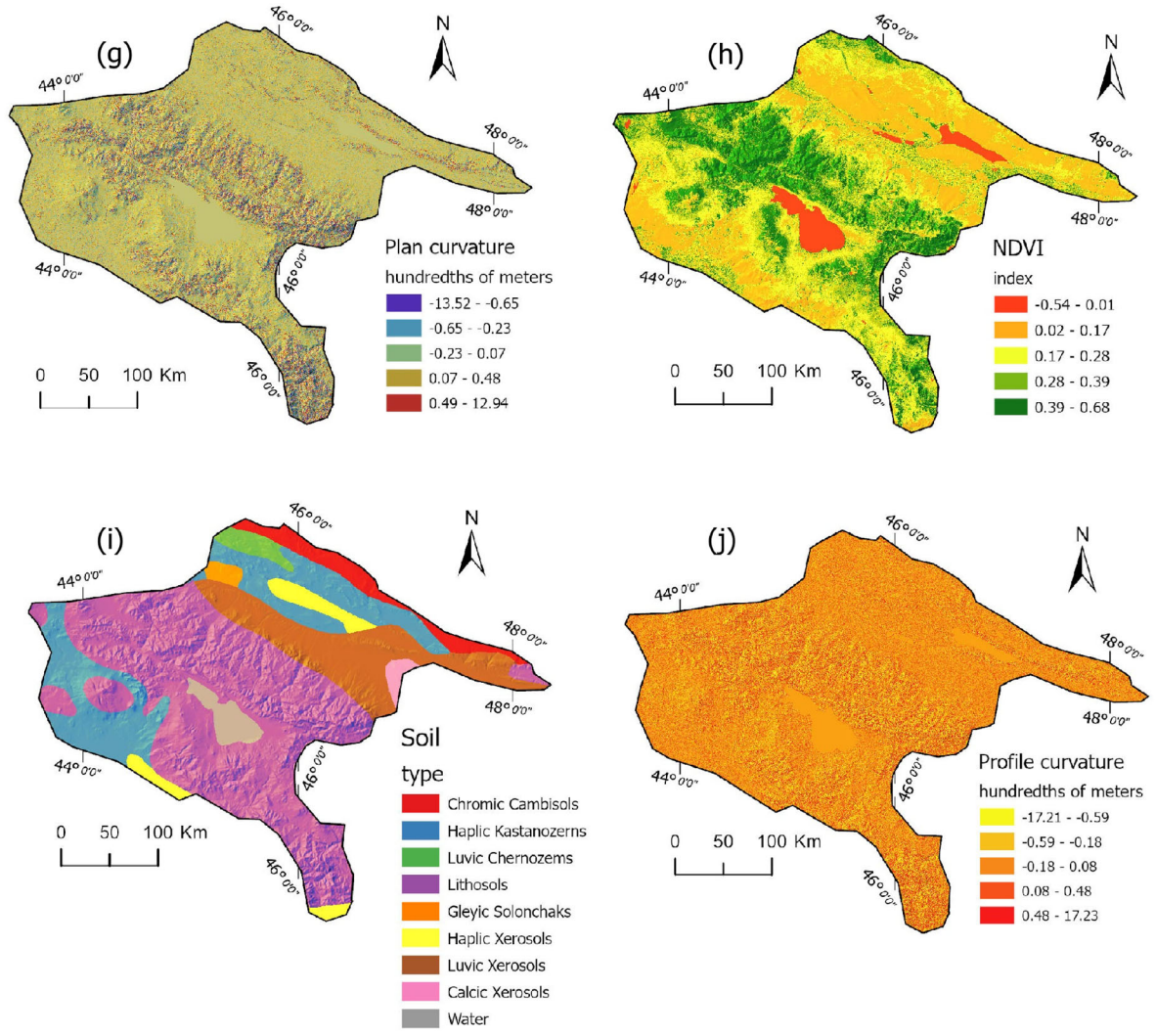

Figure 1A. Continued.